



HAL
open science

Validation of IASI satellite ammonia observations at the pixel scale using in situ vertical profiles

Xuehui Guo, Lieven Clarisse, Rui Wang, Martin van Damme, Simon Whitburn, Pierre-François Coheur, Cathy Clerbaux, Bruno Franco, Da Pan, Levi M. Golston, et al.

► To cite this version:

Xuehui Guo, Lieven Clarisse, Rui Wang, Martin van Damme, Simon Whitburn, et al.. Validation of IASI satellite ammonia observations at the pixel scale using in situ vertical profiles. *Journal of Geophysical Research: Atmospheres*, 2021, 126 (9), pp.e2020JD033475. 10.1029/2020JD033475 . insu-03115077

HAL Id: insu-03115077

<https://insu.hal.science/insu-03115077v1>

Submitted on 20 Jan 2021

HAL is a multi-disciplinary open access archive for the deposit and dissemination of scientific research documents, whether they are published or not. The documents may come from teaching and research institutions in France or abroad, or from public or private research centers.

L'archive ouverte pluridisciplinaire **HAL**, est destinée au dépôt et à la diffusion de documents scientifiques de niveau recherche, publiés ou non, émanant des établissements d'enseignement et de recherche français ou étrangers, des laboratoires publics ou privés.

1 **Validation of IASI satellite ammonia observations at the pixel scale using in-**
2 **situ vertical profiles**

3 **Xuehui Guo¹, Lieven Clarisse², Rui Wang¹, Martin Van Damme², Simon Whitburn²,**
4 **Pierre-François Coheur², Cathy Clerbaux^{2,3}, Bruno Franco², Da Pan¹, Levi M. Golston^{1,4†},**
5 **Lars Wendt⁵, Kang Sun^{1,6†}, Lei Tao^{1,7}, David Miller¹, Tomas Mikoviny^{8,9,10†}, Markus**
6 **Müller^{11,12†}, Armin Wisthaler^{11,10}, Alexandra G. Tevlin^{13,14†}, Jennifer G. Murphy¹³, John B.**
7 **Nowak^{15,16†}, Joseph R. Roscioli¹⁵, Rainer Volkamer^{17,18,19}, Natalie Kille^{17,18,19}, J. Andrew**
8 **Neuman^{18,20}, Scott J. Eilerman²¹, James H. Crawford¹⁶, Tara I. Yacovitch¹⁵, John D.**
9 **Barrick¹⁶, Amy Jo Scarino¹⁶, and Mark A. Zondlo^{1*}**

10 ¹Department of Civil and Environmental Engineering, Princeton University, Princeton, NJ, USA

11 ²Université libre de Bruxelles (ULB), Spectroscopy, Quantum Chemistry and Atmospheric
12 Remote Sensing (SQUARES), Brussels, Belgium

13 ³LATMOS/IPSL, Sorbonne Université, UVSQ, CNRS, Paris, France

14 ⁴Atmospheric Science Branch, NASA Ames Research Center, Moffett Field, CA, USA

15 ⁵Hunterdon Central Regional High School, Flemington, NJ, USA

16 ⁶Department of Civil, Structural and Environmental Engineering, University at Buffalo, Buffalo,
17 NY, USA

18 ⁷Princeton Institute for the Science and Technology of Materials, Princeton, NJ, USA

19 ⁸Chemistry and Dynamics Branch, Science Directorate, NASA Langley Research Center,
20 Hampton, VA, USA

21 ⁹Oak Ridge Associated Universities, Oak Ridge, TN, USA

22 ¹⁰Department of Chemistry, University of Oslo, Oslo, Norway

23 ¹¹Institute for Ion Physics and Applied Physics, University of Innsbruck, Innsbruck, Austria

24 ¹²Ionicon Analytik, Innsbruck, Austria

25 ¹³Department of Chemistry, University of Toronto, Toronto, Ontario, Canada

26 ¹⁴Environment and Climate Change Canada, Toronto, ON, Canada

27 ¹⁵Aerodyne Research Inc., Billerica, MA, USA

28 ¹⁶NASA Langley Research Center, Hampton, VA, USA

29 ¹⁷Department of Chemistry, University of Colorado Boulder, Boulder, CO, USA

30 ¹⁸Cooperative Institute for Research in Environmental Sciences (CIRES), University of Colorado
31 Boulder, Boulder, CO, USA

32 ¹⁹Department of Atmospheric Sciences, University of Colorado Boulder, Boulder, CO, USA

33 ²⁰NOAA Chemical Sciences Laboratory (CSL), Boulder, CO, USA

34 ²¹Jupiter Intelligence, Boulder, Colorado 80302, USA

35 † - current affiliation

36 *Corresponding author: Mark A. Zondlo (mzondlo@princeton.edu)

37

38 **Key Points:**

- 39 • IASI NH₃ columns agree well with those derived from boundary layer, in-situ
40 measurements with no significant biases at the pixel scale
- 41 • Validation in a hotspot region shows best agreement at narrow spatiotemporal scales on
42 the order of the pixel size and mean wind speed
- 43 • Additional accurate, airborne-based NH₃ datasets are critically needed for improved
44 validations across a range of environments

45

46 **Abstract**

47 Satellite ammonia (NH₃) observations provide unprecedented insights into NH₃
48 emissions, spatiotemporal variabilities and trends, but validation with in-situ measurements
49 remains lacking. Here, columns from the Infrared Atmospheric Sounding Interferometer (IASI)
50 were intercompared to boundary layer NH₃ profiles derived from aircraft- and surface-based
51 measurements primarily in Colorado, USA, in summer, 2014. IASI-NH₃ version 3 near real-time
52 dataset compared well to in-situ derived columns (windows ±15 km around centroid, ±1 hour
53 around overpass time) with good correlation ($r=0.58$), a slope near unity (0.78 ± 0.14), and an
54 intercept of $2.1\times10^{15}\pm1.5\times10^{15}$ molec cm⁻². Agreement degrades at larger spatiotemporal
55 windows, consistent with the short atmospheric lifetime of NH₃. We also examined IASI version
56 3R, which relies on temperature retrievals from the ERA Reanalysis and a third product
57 generated using aircraft-measured temperature profiles. The overall agreements improve slightly
58 for both cases. Because no bias is observed within the combined measurement errors,
59 spatiotemporal averaging of IASI over large windows can be used to reduce retrieval noise.
60 Nonetheless, sampling artifacts of airborne NH₃ instruments result in significant uncertainties of
61 the in-situ-derived columns. For example, large validation differences exist between ascent and
62 descent profiles, and the assumptions of the free tropospheric NH₃ profiles used above the
63 aircraft ceiling significantly impact the validation. Because short-lived species like NH₃ largely
64 reside within the boundary layer with complex vertical structures, more comprehensive
65 validation is needed across a wide range of environments. More accurate and widespread in-situ
66 NH₃ datasets are therefore needed for improved validations of satellite products.

67

68 **Plain Language Summary**

69 Ammonia is an important species in the atmosphere that creates particulate pollution such as
70 haze, but it is challenging to measure especially from space. Major sources of ammonia include
71 agricultural activities. Improving our estimates of the emissions require widespread and frequent
72 measurements such as those from satellite. To date, satellite-based ammonia measurements have
73 not been extensively validated, particularly on the scale of individual measurements. We have
74 compared satellite ammonia measurements with those from ground-based and aircraft
75 measurements and show that satellite measurements are accurate at the pixel scale of an

76 individual measurement. However, we also show that it is important to consider the spatial and
77 temporal differences between the measurement scales (satellite vs. ground- and aircraft-based) in
78 regions where ammonia is concentrated, and large sources exist. Improved validations will
79 require advances in airborne ammonia measurement technologies, particularly for the relatively
80 low levels of ammonia that exist above the atmospheric boundary layer. Finally, additional
81 airborne-based measurements are needed to compare to satellite-based measurements in other
82 regions and seasons to extend these results more globally.

83

84 **1. Introduction**

85 Gas-phase ammonia (NH_3) is a ubiquitous base in the atmosphere and an important
86 component of the nitrogen cycle. Atmospheric NH_3 reacts with sulfuric acid and nitric acid to
87 form ammoniated (NH_4^+) aerosol particles, reducing visibility and causing adverse effects on
88 human health (Mensink & Deutsch, 2008; Ostro *et al.*, 2015; Wang *et al.*, 2006). Ammoniated
89 aerosols also affect the climate by scattering solar radiation, resulting in a negative radiative
90 forcing (IPCC, 2013). Excess NH_3 deposited to ecosystems can cause soil acidification, water
91 eutrophication and losses of biodiversity (Galloway *et al.*, 2004). Research suggests that NH_3
92 and NH_4^+ have become increasingly important in dry and wet deposition of reactive nitrogen (N_r)
93 in most parts of the United States due to reductions in nitrogen oxides (NO_x) emissions (Li *et al.*,
94 2016).

95 Agricultural activities such as fertilizer application and livestock waste management
96 contribute to over 80% of total NH_3 emissions globally (Bouwman *et al.*, 1997; Paulot *et al.*,
97 2014). Other anthropogenic sources of NH_3 include chemical production, residential waste and
98 vehicle emissions (Behera *et al.*, 2013; Sun *et al.*, 2017; Van Damme *et al.*, 2018). Global NH_3
99 emissions are expected to increase in the forthcoming decades due to growing food demands
100 (Erisman *et al.*, 2008; Lamarque *et al.*, 2011). NH_3 is unregulated in many countries, but active
101 efforts are being made to quantify NH_3 emissions and understanding their trends and
102 distributions on regional to global scales (Paulot *et al.*, 2014; Van Damme *et al.*, 2018). There
103 remain significant uncertainties in bottom-up NH_3 emission inventories as they require
104 representative measurements to scale from a small subset of sources to the entire global budget
105 (Beusen *et al.*, 2008; Golston *et al.*, 2020; Zhang *et al.*, 2018). On the other hand, top-down
106 approaches that depend on inverse modeling of NH_4^+ wet deposition data require widespread
107 observations, accurate vertical profiles, and chemical and deposition lifetimes (Paulot *et al.*,
108 2014; Zhu *et al.*, 2013). However, current major monitoring networks such as the Ammonia
109 Monitoring Network (AMoN) in the U.S. and the Nationwide Nitrogen Deposition Monitoring
110 Network (NNDMN) in China lack the spatial coverage and temporal resolution needed to fully
111 resolve the variabilities of NH_3 , thereby introducing uncertainties in top-down estimates of NH_3
112 emissions (NADP, 2019; Xu *et al.*, 2015).

113 In the past decade, advances in remote sensing techniques have provided unprecedented
114 global coverage and medium-term time series for studying NH_3 on a broader scale not achievable
115 by ground-based measurements. Since the early 2000s, several satellites have been launched into
116 space with infrared sounders to measure atmospheric constituents. Examples of satellite NH_3
117 instruments are the Tropospheric Emission Spectrometer (TES) (Shephard *et al.*, 2011), Infrared
118 Atmospheric Sounding Interferometer (IASI) (Clarisse *et al.*, 2009; Van Damme *et al.*, 2017;
119 Whitburn *et al.*, 2016), Cross-track Infrared Sounder (CrIS) (Shephard & Cady-Pereira, 2015),

120 Atmospheric Infrared Sounder (AIRS) (Warner *et al.*, 2016) and Greenhouse Gases Observing
121 Satellite (GOSAT) (Someya *et al.*, 2019). Launched in 2004 and having ended its mission in
122 2018, TES provided the first satellite-based NH₃ product, though it only performed limited
123 measurements in its later years (Rasmussen, 2018). IASI provides Level-2 (L2) NH₃ products
124 dating back to 2008 with much broader spatial coverage than TES. AIRS has the longest data
125 record of NH₃ on a single satellite between 2002 and 2016 (Warner *et al.*, 2017). CrIS and
126 GOSAT are more recently developed NH₃ products with limited availability at this time
127 (Dammers *et al.*, 2019).

128 Despite the increasing use of satellite NH₃ products for inventory assessments, nitrogen
129 deposition, and aerosol chemistry, validations of satellite NH₃ measurements, especially those
130 against independent in-situ measurements, remain limited (Dammers *et al.*, 2019; Van Damme *et*
131 *al.*, 2018; Zhang *et al.*, 2018). Although averaged satellite data over a large domain can be used
132 to study regional and global characteristics of NH₃, validations of individual satellite pixels help
133 further understand the capabilities and constraints of satellite observations. Meanwhile, analyses
134 of satellite NH₃ on fine temporal (e.g. daily and weekly) and local scales, such as fertilizer
135 emissions, require validation for increased confidence (Fortems-Cheiney *et al.*, 2016; Van
136 Damme *et al.*, 2018). Previously, Van Damme *et al.* (2015) used an averaged GEOS-Chem
137 model profile to convert IASI NH₃ columns into surface concentrations and found fair
138 agreements between IASI and ground-based observations on monthly scales, and moderate
139 correlations with hourly airborne data, but the fixed profile shapes used for the conversion
140 introduced certain biases in IASI surface concentration estimations. Dammers *et al.* (2016)
141 validated IASI using column measurements from ground-based high-resolution Fourier-
142 transform infrared spectroscopy (FTIR) at nine locations worldwide with spatial and temporal
143 windows of 25 km and 90 min, respectively. Good agreements ($r \sim 0.8$) were found where NH₃
144 levels were high, though the study removed outliers during wintertime. In addition, the FTIR
145 measurements themselves have not been validated by in-situ profiles and instead rely upon
146 model a priori and limited surface observations (Dammers *et al.*, 2015). Similarly, a comparison
147 between CrIS and FTIR was conducted by Dammers *et al.* (2017), where an overall good
148 correlation was observed, but the agreements for individual sites varied largely. Using a different
149 method, Sun *et al.* (2015) conducted a validation of TES NH₃ with collocated aircraft and mobile
150 lab measurements in California at the pixel scale and found the agreement to be within 10% for
151 selected dates. Furthermore, the spatial variability of NH₃ columns within a satellite pixel (IASI:
152 ~ 12 km in diameter) has been assessed over Colorado using structure functions analyses of
153 mobile NH₃ column observations conducted on fine spatial scales (few 10 meters; Follette-Cook
154 *et al.*, 2015; Kille *et al.*, 2017). During the time of this study, Kille *et al.* (2017) found 50% of
155 variability in NH₃ columns at distances less than approximately 1.6 km, and 90% of variability at
156 distances less than 6 km. The high atmospheric NH₃ variability poses a fundamental sampling
157 challenge to satellite validation on the pixel scale and illustrates the need for a multi-platform
158 sampling strategy for best results.

159 To expand the scope and robustness of satellite NH₃ validations, we compare the IASI
160 NH₃ at the pixel scale with a combination of aircraft-based profiles and an assortment of other
161 in-situ and mobile column surface observations taken during the summer of 2014 in Colorado,
162 USA, with some insight on the winter of 2013 in California, USA. The general approach used
163 here can be readily applied to other satellite NH₃ products, provided that NH₃ vertical profiles
164 are nearly collocated with the satellite pixels within a temporal window that is consistent with
165 wind and atmospheric transport.

166 2. Data and Methods

167 2.1. IASI Observations

168 IASI is an infrared sounder onboard the polar-orbiting Metop-A/B/C satellites, which
169 were respectively launched in 2006, 2012 and 2018 (Clerbaux *et al.*, 2009). It is sensitive to NH₃
170 absorption features mainly between 800 and 1200 cm⁻¹ (Clarisse *et al.*, 2010; Coheur *et al.*,
171 2009). IASI provides twice-daily measurements of NH₃ with overpass times of 0930/2130 local
172 solar time (LST). IASI has a swath of 2400 km and a pixel size of 12 km in diameter at nadir.
173 The first IASI NH₃ product was retrieved using lookup tables (LUTs) based on simulations from
174 a forward radiative transfer model. A hyperspectral range index (HRI) was calculated from each
175 observation and converted to NH₃ columns using the LUTs (Van Damme *et al.*, 2014). A
176 subsequent version (ANNI-NH3-v1) improved the retrieval of NH₃ by using an artificial neural
177 network for IASI (ANNI) to transform the calculated HRI into column densities (Whitburn *et al.*,
178 2016). Version 2 of the ANNI product further improved the algorithm by introducing separate
179 neural networks for land and sea, and simplified input parameters. With the release of this
180 version, an additional product was made available using meteorological retrievals from the
181 European Centre for Medium-Range Weather Forecasts Re-Analysis (ERA)-Interim ECMWF
182 for better interannual consistency, as opposed to using meteorological data from IASI itself to
183 calculate columns (Van Damme *et al.*, 2017). It is emphasized that the ANNI-NH₃ products do
184 not produce information on averaging kernel (AVK) because the current retrieval method is not
185 based on optimal estimation (Whitburn *et al.*, 2016). Thus, only the unconstrained columns were
186 used here to provide an overview of the agreement between IASI and in-situ measurements.

187 In this work, we analyze version 3 of the ANNI-NH₃ product from IASI Metop-A/B. This
188 version, processed using the retrieval framework outlined in (Franco *et al.*, 2018), features a
189 slightly increased measurement sensitivity due to small changes in the neural network
190 architecture and training and improved post-filtering. In addition, several debiasing procedures
191 have been introduced to correct for the gradual increase of CO₂ columns over the entire IASI
192 time-period and for IASI instrument calibrations. Despite the significant number of changes from
193 v2 to v3, the changes to the retrieved columns are modest in the mean. For columns above
194 4×10^{15} molec cm⁻², 80% of the data agree to within 20%. As infrared retrievals are known to be
195 quite sensitive to auxiliary input data, we evaluate the following products: (1) The near real-time
196 product, retrieved using meteorological data from the European Organisation for the Exploitation
197 of Meteorological Satellites (EUMETSAT) with cloud coverage < 25%, (2) the reanalysis
198 product, retrieved using meteorological data from ERA5/ECMWF with cloud coverage < 10%,
199 and (3) a dedicated product retrieved using collocated in-situ temperature profiles from aircraft,
200 sonde and mobile measurements (other meteorological data such as skin temperature are from
201 EUMETSAT) with cloud coverage < 25%. We only include the morning observations over land
202 surfaces as IASI has better sensitivity to NH₃ under these conditions.

203 2.2. In-situ Measurements

204 The Deriving Information on Surface conditions from Column and Vertically Resolved
205 Observations Relevant to Air Quality (DISCOVER-AQ) field experiment was a multi-year
206 campaign led by the National Aeronautics and Space Administration (NASA) (Crawford &
207 Pickering, 2014). Its mission was to validate collocated satellite observations of atmospheric

208 pollutants over four regions in the U.S. (Baltimore/Washington, California, Houston, and
209 Colorado). Airborne NH₃ measurements were only available in the California and Colorado
210 campaigns, the foci of this study. The California campaign occurred between January 16 and
211 February 7, 2013 over the San Joaquin Valley. In the following year, the experiment was
212 continued in Colorado from July 16 to August 16, along with a complimentary National Science
213 Foundation (NSF) Front Range Air Pollution and Photochemistry Experiment (FRAPPÉ) that
214 had additional platforms and NH₃ measurements (Flocke *et al.*, 2020). The DISCOVER-AQ
215 flight patterns were specifically designed for satellite validations as the P-3B aircraft made
216 repeated upward and downward spirals at several designated locations for the construction of
217 vertical profiles. A typical P-3B spiral roughly spanned 5 km in diameter, which were
218 particularly advantageous for validations of short-lived species such as NH₃ that exhibits strong
219 spatial gradients near source regions.

220 A unique aspect of the 2014 Colorado campaign compared to past field experiments was
221 the comprehensive suite of NH₃ measurements on multiple platforms: two aircraft, a tall tower,
222 and four mobile laboratories. The NASA P-3B aircraft measured NH₃ with a proton-transfer
223 time-of-flight mass spectrometer (Müller *et al.*, 2014). The NSF/NCAR C-130 aircraft measured
224 NH₃ with a closed-path, quantum cascade laser-based instrument using a fast-response inertial
225 inlet to minimize sampling artifacts (QC-TILDAS, Aerodyne Research Inc.) (Schiferl *et al.*,
226 2016). A moving carriage on the Boulder Atmospheric Observatory's (BAO) 300 m tall tower in
227 Erie, Colorado made profiles every hour and was equipped with a closed-path, quantum cascade
228 laser-based NH₃ instrument (QC-TILDAS, Aerodyne Research Inc.) (Tevlin *et al.*, 2017). The
229 mobile laboratories included in-situ measurements from an open-path, quantum cascade laser-
230 based instrument onboard the Princeton Atmospheric Chemistry Experiment, a cavity ring down
231 instrument (Picarro G2103) onboard the NOAA Chemical Sciences Division (CSD) van, and a
232 closed-path, quantum cascade laser-based instrument (QC-TILDAS) on the Aerodyne Mobile
233 Laboratory (Eilerman *et al.*, 2016; Herndon *et al.*, 2005; Tao *et al.*, 2015). These three mobile
234 laboratories conducted a stationary and moving intercomparison and showed agreement to within
235 10% on average (Golston *et al.*, 2020). Column NH₃ abundances were measured by the
236 University of Colorado Solar Occultation Flux (CU SOF) instrument onboard the CU/NCAR
237 mobile laboratory (Kille *et al.*, 2017). CU SOF couples a digital fast solar tracker (Baidar *et al.*,
238 2016; Patent No. 10379194, 2019) to a fast scanning FTIR to measure the vertical column
239 integral of NH₃ and other gases above the mobile platform directly in the open atmosphere (Kille
240 *et al.*, 2017). Table 1 summarizes the performances of the NH₃ instruments during the two
241 campaigns.

242 In addition to the NH₃ measurements, temperature and pressure measurements were taken
243 from the P-3B aircraft and specially launched radiosondes (iMet-1 & Vaisala RS92) timed with
244 aircraft flights. These data allowed for the construction of in-situ derived NH₃ columns and for
245 the generation of IASI NH₃ measurements with in-situ temperature measurements as input. For
246 the determination of atmospheric mixed layer height (MLH) used in the construction of in-situ
247 NH₃ profiles, we examined P-3B aircraft profiles of other short-lived species with sources in this
248 region including nitrogen dioxide (NO₂) (Weinheimer *et al.*, 1994), ethane (C₂H₆) from gas-oil
249 activities (Yacovitch *et al.*, 2014), and the number concentration of particles (CN) with diameters
250 > 10 nm from the LARGE instrument (Beyersdorf *et al.*, 2016). Additional MLH measurements
251 were incorporated from the High Spectral Resolution LIDAR (HSRL2) instrument onboard the

252 NASA B200 aircraft (Scarino *et al.*, 2014). Table 2 lists the dates on which each platform was
 253 functional during these campaigns.

254 **Table 1.** Summary of in-situ NH₃ measurements during DISCOVER-AQ

Platform	Method	Typical uncertainty	Referenced Work
California (2013)			
NASA P-3B aircraft	PTR-MS	± 35%	(Müller <i>et al.</i> , 2014)
NASA P-3B aircraft	CRDS	± (35% + 1.7 ppbv) + 0.2 ppbv ^a	(Schiferl <i>et al.</i> , 2016)
Princeton mobile	Open-path QCL	± 20%	(Miller <i>et al.</i> , 2015)
Colorado (2014)			
NASA P-3B aircraft	PTR-MS	± 35%	(Müller <i>et al.</i> , 2014)
NSF/NCAR C-130 aircraft	QC-TILDAS	± (22% + 0.305 ppbv) + 0.058 ppbv ^a	(Ellis <i>et al.</i> , 2010; Schiferl <i>et al.</i> , 2016)
Aerodyne mobile	QC-TILDAS	± (22% + 0.305 ppbv) + 0.058 ppbv ^a	(Ellis <i>et al.</i> , 2010; Schiferl <i>et al.</i> , 2016)
Princeton mobile	Open-path QCL	± 10% + 0.2 ppbv ^a	(Miller <i>et al.</i> , 2014; Tao <i>et al.</i> , 2015)
CU/NCAR mobile	SOF	± 4.4% + 1×10 ¹⁵ molec cm ⁻² a	(Kille <i>et al.</i> , 2017)
NOAA CSD mobile	CRDS	± 20% + 1 ppbv ^a	(Eilerman <i>et al.</i> , 2016)
NOAA BAO tower	QC-TILDAS	± 20% + 0.5 ppbv ^a	(Tevlin <i>et al.</i> , 2017)

255 *Note.* PTR-MS = proton transfer reaction-mass spectrometer; CRDS = cavity ring down
 256 spectrometer; QCL = quantum cascade laser; NSF = National Science Foundation; NCAR =
 257 National Center for Atmospheric Research; QC-TILDAS = quantum cascade tunable infrared
 258 laser direct/differential absorption spectroscopy; CU = University of Colorado; SOF = Solar
 259 Occultation Flux. BAO = Boulder Atmospheric Observatory. Uncertainties are presented as
 260 reported in archived field data catalog and/or related publications. Subscripts in the third column:
 261 ^a uncertainty + limit of detection.

262 **Table 2.** Availability of in-situ NH₃ measurements in DISCOVER-AQ California in 2013 (upper
 263 table) and Colorado in 2014 (lower table). Colored and blank cells represent dates when data
 264 from each platform were or were not available, respectively.

Platform	Date																			
	1/16	1/17	1/18	1/19	1/20	1/21	1/22	1/25	1/26	1/27	1/28	1/29	1/30	1/31	2/1	2/3	2/4	2/5	2/6	2/7
NASA P-3B (PTR-MS, A. Wisthaler)																				
NASA P-3B (CRDS, J. Nowak & A. Neuman)																				
Princeton mobile (Open-path QCL, M. Zondlo)																				

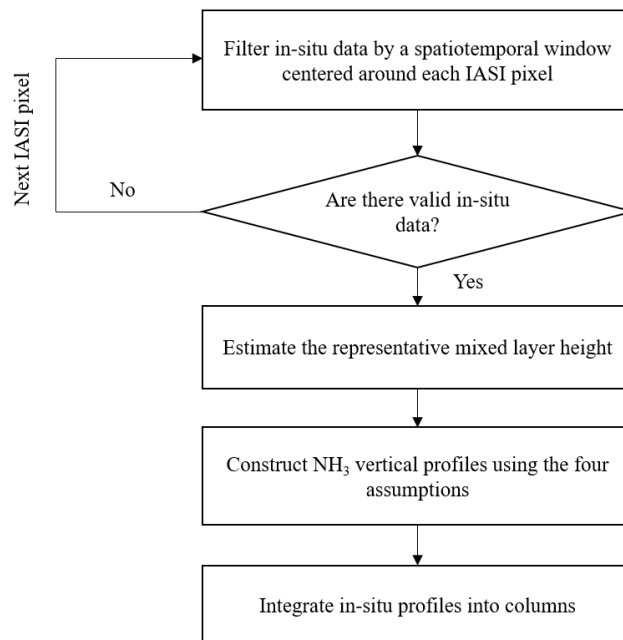
265

Date Platform	7/16	7/17	7/18	7/19	7/20	7/21	7/22	7/23	7/24	7/25	7/26	7/27	7/28	7/29	7/30	7/31	8/1	8/2	8/3	8/4	8/5	8/6	8/7	8/8	8/9	8/10	8/11	8/12	8/13	8/14	8/15	8/16	8/18		
NASA P-3B (PTR-MS, A. Wisthaler)																																			
NCAR/NSF C-130 (QC-TILDAS, S. Herndon, R. Roscioli, J. Nowak,)																																			
Aerodyne mobile (QC-TILDAS, C. Floerchinger)																																			
Princeton mobile (Open-path QCL, M. Zondlo)																																			
CU mobile (SOF-FTIR, R. Volkamer)																																			
NOAA CSD mobile (CRDS, A. Neuman)																																			
NOAA BAO tower (QC-TILDAS, J. Murphy)																																			

266 2.3. Validation Algorithm

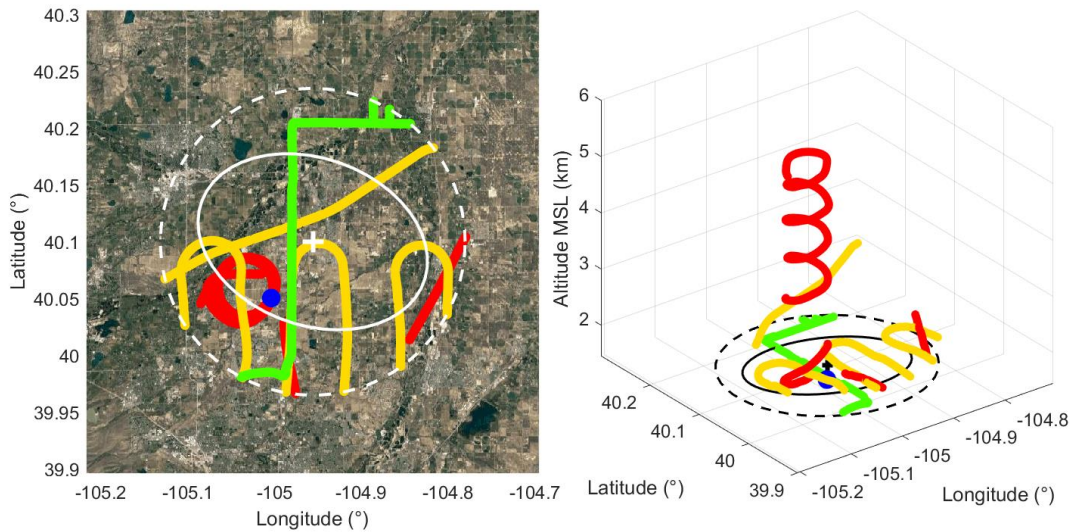
267 2.3.1. Spatiotemporal filtering

268 The general framework of the validation algorithm used in this study is shown in Figure
 269 1. For each valid IASI observation, we applied a spatiotemporal window centered on the pixel's
 270 center location and overpass time to filter for DISCOVER-AQ data within the designated
 271 window. For example, if an in-situ measurement was made inside a certain spatial distance (e.g.
 272 ± 15 km) from the center of the IASI pixel, and the time difference relative to the IASI overpass
 273 time was within the temporal window (e.g. ± 60 min), the measurement was considered valid for
 274 comparison. This applied to all in-situ NH_3 measurements and other relevant data (e.g.
 275 radiosondes). The only exception was the P-3B aircraft profiles, where we included all the data
 276 in a vertical profile if the geographical center (mean latitude and longitude) of the aircraft spiral
 277 fell inside the spatial window. Next, in-situ NH_3 measurements located within the spatiotemporal
 278 window were aggregated into one dataset. Each collocation between IASI and in-situ
 279 measurements required at least one aircraft profile available so that an NH_3 vertical profile could
 280 be constructed. Figure 2 shows an example of collocation between IASI and in-situ
 281 measurements on July 27, 2014. The location of IASI pixel centroid, denoted as a "+", is
 282 positioned in the center with its footprint boundary outlined as a solid white ellipse. The spatial
 283 window (in this case, ± 15 km) is plotted as a dotted white circle. For demonstration purposes, the
 284 ± 3 hour temporal window is chosen to include as many measurements as possible. The route of
 285 each in-situ platform is marked with a different color. In this example, in-situ NH_3 measurements
 286 were available from P-3B, C-130, Princeton mobile lab and BAO tower.



287
 288 **Figure 1.** Overview of the validation algorithm. The flowchart is repeated for each valid IASI
 289 pixel. If no in-situ data are found near the pixel, the pixel will be skipped, and the next available
 290 pixel will be scanned for collocation. The four scenarios in box 4 are described in section 2.3.2
 291 and illustrated with an example in Figure 3.

292



293

294 **Figure 2.** Example of collocated IASI and in-situ measurements on July 27, 2014 at 17:34:09
 295 UTC. The left panel shows a two-dimensional view from the top and the right panel visualizes
 296 the movements of the in-situ platforms in a three-dimensional view. The center of the IASI pixel
 297 is denoted as “+”. The solid ellipse marks the boundary of the IASI pixel. The dotted circle
 298 represents the ± 15 km spatial window. The temporal window is ± 3 hour in this case. Colored
 299 lines show the routes of the in-situ platforms: red = P-3B, yellow = C-130, green = Princeton
 300 mobile lab, blue dot = BAO tower. The 2D figure is overlaid on Google Maps (Google, Inc.) for
 301 better visualization of the geographical location and topography.

302 2.3.2. Reconciling uncertainties in NH_3 profiles

303 The combined in-situ dataset was then used to calculate the integrated column density of
 304 NH_3 . Two issues remained, however, in the construction of the in-situ-derived columns. First,
 305 because the aircraft ceiling on most spirals was limited to ~ 5 km above sea level, it was
 306 necessary to assume NH_3 concentrations in the middle and upper troposphere. Even though NH_3
 307 is expected to accumulate mostly in the boundary layer because of its short-lifetime on the order
 308 of hours to days (Dentener & Crutzen, 1994; Seinfeld & Pandis, 2016), NH_3 has been measured
 309 in the middle and upper troposphere previously (Whitburn *et al.*, 2016). Höpfner *et al.* (2016) for
 310 instance measured NH_3 levels in the upper troposphere to be tens of parts per trillion by volume
 311 ($1 \text{ pptv} = 10^{-12} \text{ mol/mol}$) in the outflow of the active Monsoon system. However, the free
 312 tropospheric NH_3 background was below the detection limit ($< 3\text{-}5 \text{ pptv}$). More recently,
 313 Höpfner *et al.* (2019) found that NH_3 concentrations in the upper troposphere could reach up to 1
 314 ppbv in some regions during the Asian monsoon season, but were low in most other places.
 315 Other studies that measured NH_3 profiles showed sharp decreases of NH_3 mixing ratio over
 316 altitude (Nowak *et al.*, 2010), and low NH_3 ($< 1 \text{ ppbv}$) at similar altitudes (Hoell *et al.*, 1980;
 317 Ziereis & Arnold, 1986). Based on this evidence, it is reasonable to argue that NH_3
 318 concentrations in the upper troposphere are negligible compared to the lower troposphere.
 319 Second, a problem remained on how to deal with NH_3 concentrations measured by the aircraft
 320 beyond the MLH. Previously, Sun *et al.* (2015) found that airborne NH_3 sensors (i.e. Picarro

321 CRDS and PTR-MS on the P-3B aircraft) in DISCOVER-AQ California exhibited sampling
322 artifacts above the MLH due to long and variable instrument response times. Because
323 DISCOVER-AQ CA and CO were in agricultural source regions, a strong gradient existed from
324 very high levels within the boundary layer to nominally-clean free tropospheric levels. Such
325 strong gradients can be problematic for accurately quantifying NH_3 with an instrument or inlet
326 that has a time response slower than the rapid changes in ambient mixing ratios (Fehsenfeld *et*
327 *al.*, 2002; Von Bobruzki *et al.*, 2010).

328 Given these issues on the column construction from the aircraft data, we accounted for
329 the lack of a full tropospheric profile, and sampling artifacts, by bracketing four possible
330 scenarios of NH_3 distributions above the MLH in the troposphere. Figure 3 shows the case
331 studies used to address the vertical profile in the free troposphere: (1) integrating NH_3 only up to
332 the MLH, assuming negligible NH_3 concentrations above. Physically, this corresponds to the
333 assumption that NH_3 is contained within the boundary layer and dominates the column
334 measurement based on its short lifetime. It also assumes that sampling biases of instruments are
335 large in and around the strong gradient of the mixed layer. (2) Integrating NH_3 up to the
336 maximum aircraft altitude, assuming negligible NH_3 at altitudes higher than the aircraft ceiling.
337 This assumes that aircraft NH_3 measurements above the MLH are valid and real signals, but no
338 extrapolation is done beyond the aircraft range. (3) Integrating NH_3 up to the tropopause with
339 linear interpolation of decreasing mixing ratios from the maximum aircraft altitude to zero at the
340 tropopause estimated from sonde temperature profiles. In the real atmosphere, NH_3 is removed
341 from the atmosphere by reacting with nitric and sulfuric acids, and through dry deposition in the
342 gas phase and wet deposition as NH_4^+ by cloud scavenging (Mensink & Deutsch, 2008; Mizak *et*
343 *al.*, 2005; Nemitz, Milford, & Sutton, 2001). The linear interpolation represents a simplistic
344 mode of decay of NH_3 concentrations over altitude via the removal pathways. (4) Integrating
345 NH_3 up to the tropopause, while assuming constant NH_3 mixing ratio from the maximum aircraft
346 altitude to the tropopause. The last scenario features a well-mixed free troposphere in which NH_3
347 distributes uniformly in the vertical direction. In all four scenarios, we assumed NH_3 was
348 negligible further beyond the tropopause based on previous studies (Höpfner *et al.*, 2019, 2016).
349 While the truth is not likely to be any of these exact scenarios, these case studies of the free
350 tropospheric NH_3 distribution helped to bracket the magnitude and importance of the full NH_3
351 vertical profile that was not captured by the aircraft or caused by potential sampling problems in
352 the in-situ measurements.

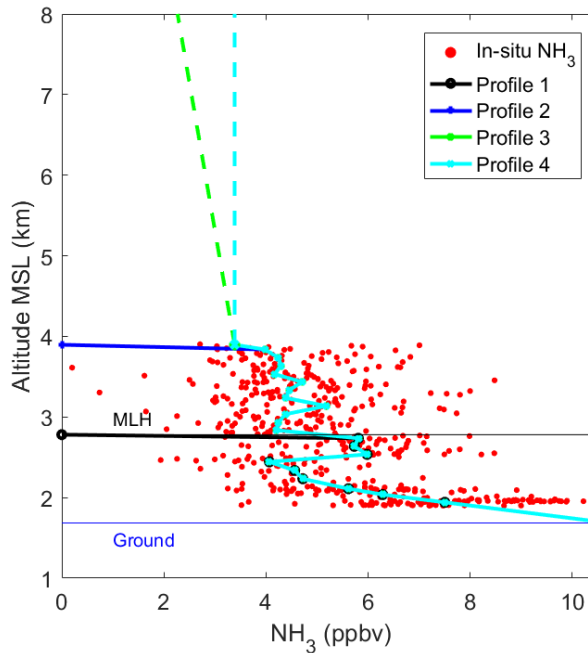
353 Knowing the representative MLH for each collocation was necessary for the integration
354 of NH_3 profile in the first case. We estimated the MLH using three methods to minimize
355 potential errors and mismatches due to geographical elevation differences within the window: (1)
356 using the altitude of the first inversion of the temperature profile from the nearest timed sonde
357 launch (which may not necessarily be in the exact spatiotemporal window), (2) using aerosol
358 backscatter data from the B200 aircraft within the specified spatiotemporal window, and (3)
359 derived from the vertical profiles of other, short-lived atmospheric tracers (NO_2 , C_2H_6 and $\text{CN} >$
360 10 nm) measured by P-3B. The final MLH was calculated as the average of all available methods
361 for each collocation.

362 2.3.3. Vertical integration

363 The available in-situ NH_3 measurements at 1 Hz were vertically binned every 100 m to
 364 reduce noise, and the median value in each layer was used to build the final vertical profiles.
 365 Median values were chosen because in-situ measurements on or near the ground immediately
 366 downwind of sources (e.g. feedlots) would skew the mean to be unrepresentative of the overall
 367 layer. When there was an altitude mismatch between the lowest in-situ bin and the ground at the
 368 pixel's center location (i.e. in-situ altitude > IASI centroid altitude), the NH_3 mixing ratio at the
 369 ground level was linearly extrapolated to the ground from the lowest bin. In cases where the
 370 IASI centroid ground altitude was higher than in-situ locations, only measurements higher than
 371 the ground altitude were included. Using the ideal gas law, the column NH_3 was integrated from
 372 gas density over altitude:

$$373 \quad \omega_{\text{NH}_3} = \int \frac{C_{\text{NH}_3} P_{\text{air}}}{k T_{\text{air}}} dz$$

374 where ω_{NH_3} is the column density of NH_3 in the same unit as IASI (molec cm^{-2}), C_{NH_3} is
 375 the mixing ratio of NH_3 in air, P_{air} is the air pressure, k is the Boltzmann's constant, T_{air} is the
 376 air temperature, and z is the altitude.



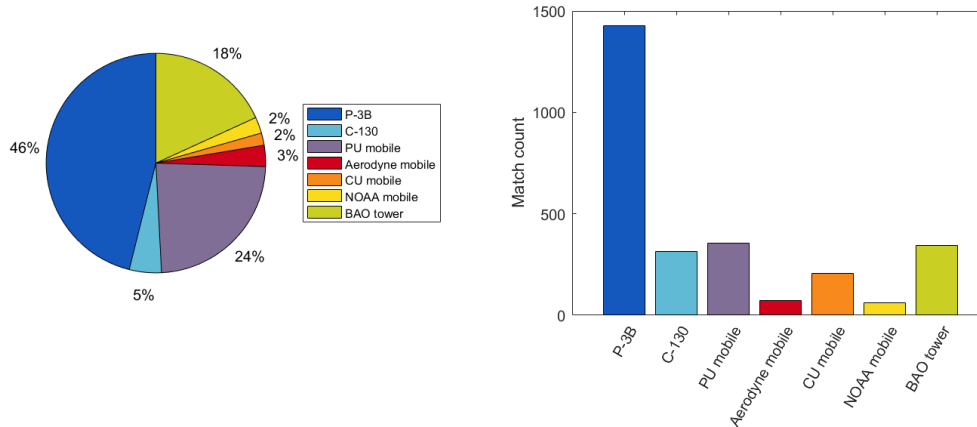
377
 378 **Figure 3.** Four assumed NH_3 vertical profiles in this work. Profile 1 (black): integration up to
 379 MLH with zero NH_3 above; Profile 2 (dark blue): integration up to maximum aircraft altitude
 380 and zero NH_3 above; Profile 3 (green): integration up to tropopause with linear interpolation of
 381 concentrations beyond aircraft altitudes to a value of zero at the tropopause; Profile 4 (turquoise):
 382 integration up to tropopause assuming constant NH_3 beyond aircraft altitude. The median profile
 383 from each assumption is shown with the interpolated sections above the aircraft altitude plotted
 384 as dashed lines. In-situ NH_3 concentrations at 1 Hz are colored in red. The thin blue line

385 indicates the ground altitude at the IASI pixel center. The thin black line denotes the
386 corresponding MLH in this case. Altitude MSL stands for altitude above mean sea level.

387 The in-situ temperature profiles used for generating the alternative IASI-NH₃ product
388 described in section 2.1 were aggregated from the in-situ platforms in section 2.2 and filtered
389 using the spatiotemporal window of interest. Sonde measurements of temperature were needed to
390 fill in the gap of aircraft temperature measurements (e.g. near the ground, above the ceiling), yet
391 in many cases a sonde could not be found within the window. Therefore, we always used the
392 nearest sonde in time to construct the temperature profile, whether it was located within the
393 specified spatial window. In California, however, this approach was not ideal in winter. Due to
394 strong yet shallow inversions, there were often large discrepancies between the sonde
395 temperatures and those measured by the aircraft, especially near the surface. To reduce errors
396 due to separation in distance, we used P-3B aircraft temperatures where applicable and sonde
397 measurements outside the aircraft altitude range for California. In Colorado in summer, the
398 horizontal gradients of temperature were less pronounced, and temperature profiles measured by
399 P-3B and a given sonde usually matched up very well. Therefore, temperature data from the two
400 platforms were integrated together, while we further combined them with ground measurements
401 of temperature (e.g. mobile labs) if available. The merged temperatures were grouped in bins of
402 100 m, and the mean value in each bin was used to make the final temperature profile.

403 2.3.4. Data coverage

404 We quantify data coverage contributions from each in-situ platform to the validation
405 dataset using two approaches: (1) by the sum of total measurement time, and (2) by the number
406 of cases when the platform collocated with IASI. Some measurements were counted more than
407 once if they were found to collocate with IASI in multiple windows that we tested. Figure 4
408 shows that the P-3B aircraft that carried the PTR-MS instrument was the largest contributor to
409 the in-situ dataset in Colorado, because we required each IASI-in-situ collocation to have an
410 aircraft profile from P-3B (the C-130 aircraft, on the other hand, did not perform vertical profiles
411 at fixed locations). The Princeton mobile lab and the BAO tower were operational on most days
412 and became the next major contributors. Although each in-situ NH₃ instrument has a different
413 uncertainty estimate (Table 1), we applied a 30% error to the entire in-situ dataset to approximate
414 the overall instrument uncertainty. Because of potential systematic biases in the in-situ
415 measurements, we did not use a weighted average of errors from different measurements within
416 a given profile layer. Instrument biases were thought to be the limiting factors of the uncertainty
417 in all the in-situ measurements of NH₃ mixing ratio, and unlike random errors, these would not
418 be reduced through averaging.



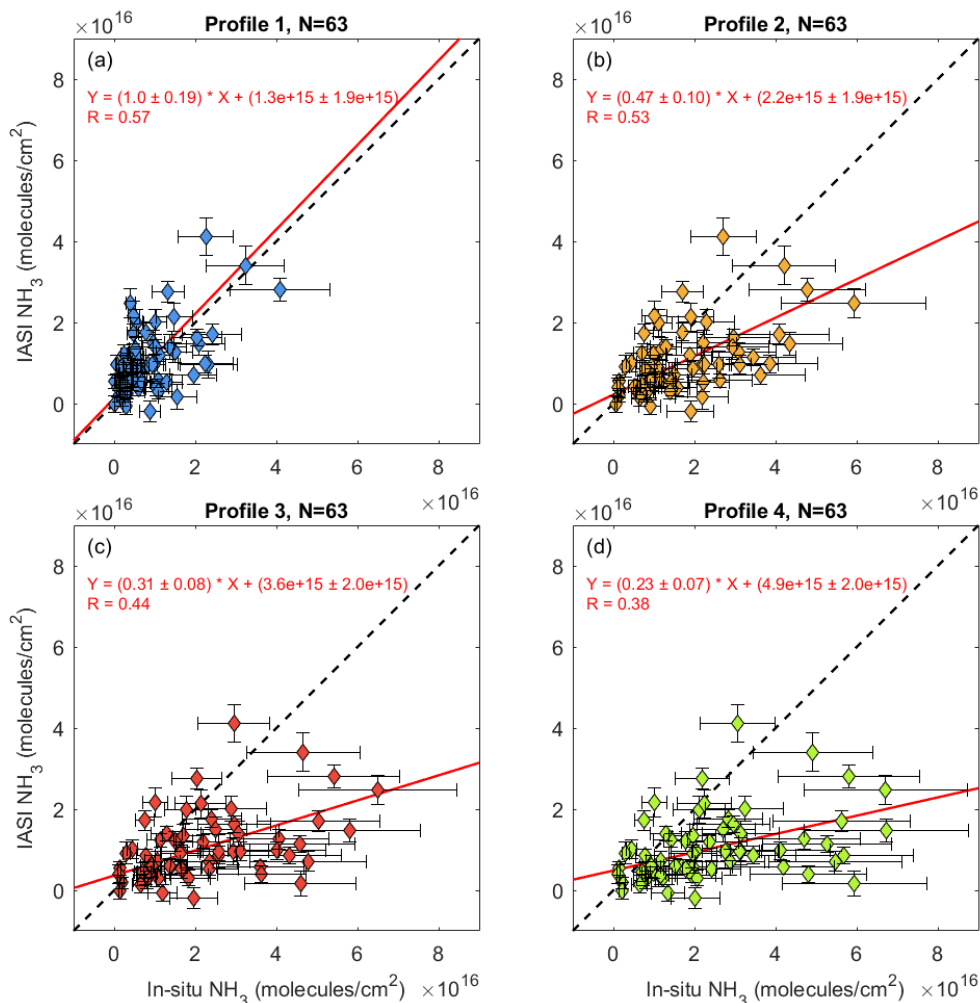
419

420 **Figure 4.** Data contribution from each in-situ platform in DISCOVER-AQ Colorado by (a) sum
 421 of total measurement time and (b) number of cases collocated with IASI. Statistics shown here
 422 are for all nine spatiotemporal windows tested in this study (total count of collocations = 1,426).

423 3. Results and Discussion

424 3.1. Comparison between Different In-situ Profiles

425 The four different scenarios of NH_3 profiles were quantitatively evaluated and compared
 426 based on the data in Colorado, given the larger suite of measurements in this campaign. For
 427 comparison purposes, we only show the comparison between in-situ and the reanalysis IASI
 428 product, but the overall conclusion holds true for the other two IASI products as well. The IASI
 429 reanalysis product versus the four in-situ profiles are plotted in Figure 5 with an orthogonal
 430 linear regression fit (MATLAB R2016b, MathWorks) that accounts for uncertainties in both the
 431 abscissa and ordinate variables. Profile 1 leads to the lowest column abundance among the four
 432 profiles because all the NH_3 measurements above the MLH are excluded. The column
 433 abundances increase sequentially from profile 1 to 4 as the contributions from the free
 434 troposphere increase. The correlation coefficient and slope between IASI and in-situ in Colorado
 435 indeed show a sequential degradation from profile 1 to 4 as extra NH_3 is added into the
 436 integration. We hypothesized in section 2.3 that the MLH assumption (profile 1) would be the
 437 closest representation of vertical distributions of NH_3 in the real atmosphere based on its short
 438 lifetime, emissions at the surface, and negligible amounts measured elsewhere in the free
 439 troposphere. Profile 1 shows the overall best agreement between IASI and in-situ, and this is
 440 consistent with the expectation that most NH_3 is accumulated within the boundary layer. We note
 441 that profile 2, which treats all aircraft data as valid, shows a similar correlation (though a factor
 442 of two difference in the slope). However, there are potential caveats associated with using the
 443 airborne measurements above the MLH given the sampling artifacts, which will be further
 444 discussed in section 3.5. All the correlations shown are tested to be statistically significant
 445 ($p < 0.05$, same for all the analyses onward).



446

447 **Figure 5.** Reanalysis IASI product versus in-situ integrated columns from the four profiles for
 448 the ± 15 km and ± 60 min in Colorado. Profile 1: integration up to MLH; Profile 2: integration up
 449 to maximum aircraft altitude; Profile 3: integration up to tropopause assuming a linearly
 450 decreasing NH_3 mixing ratio beyond aircraft altitude; Profile 4: integration up to tropopause
 451 assuming constant NH_3 beyond aircraft altitude. Error bars indicate the uncertainties of columns.

452

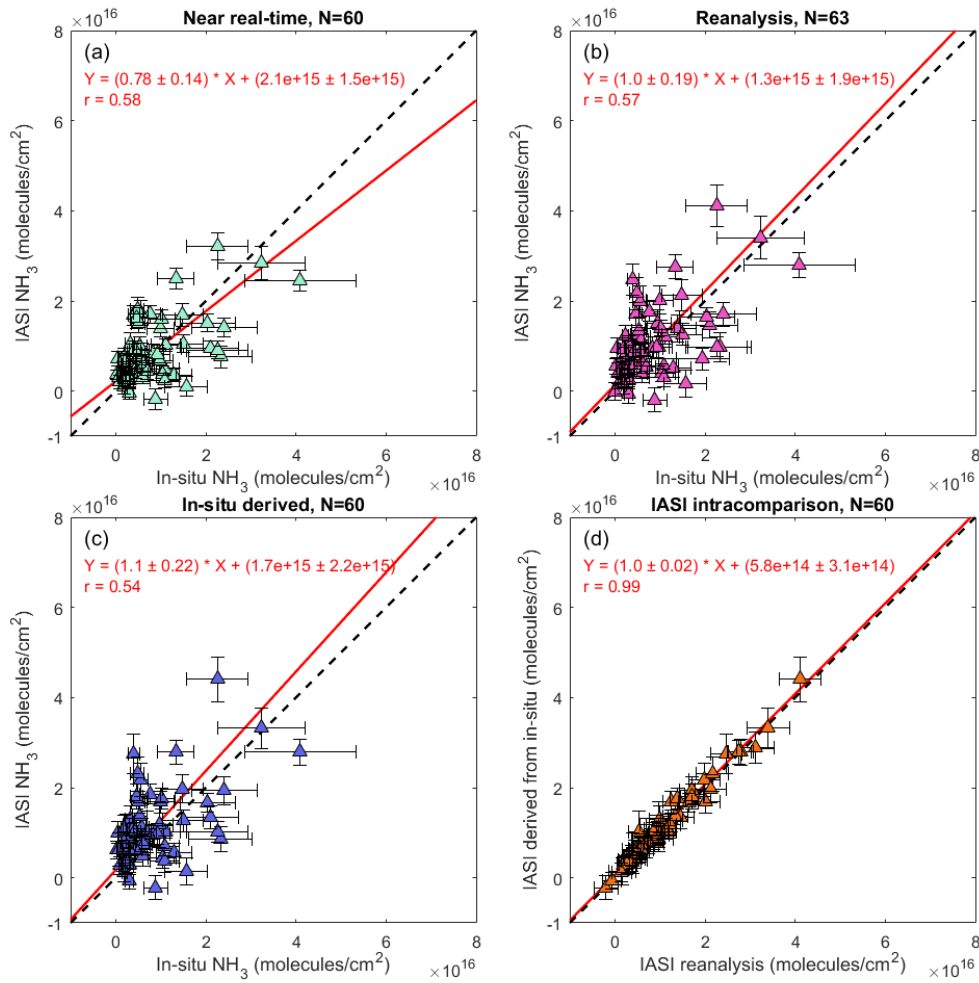
3.2. Comparison between Different IASI Products

453 The three IASI products described in section 2.1 were compared with vertically
 454 integrated in-situ columns under the MLH assumption (profile 1) within the ± 15 km and ± 60 min
 455 window in Colorado (Fig. 6). We determined the optimal size of the spatiotemporal window
 456 based on wind speeds in the boundary layer. To calculate typical boundary layer wind speeds, we
 457 used wind data measured at 300 m on the BAO tower located in Erie, CO (40.050° N, 105.004°
 458 W) from 0600-1200 local time during DISCOVER-AQ to bracket the IASI overpass times,
 459 which are always in the morning. The average wind speed during the campaign was $3.5 \pm 2.2 \text{ m s}^{-1}$
 460 (median: 3.1). The mean value is equivalent to a spatial window of approximately 15 km in
 461 diameter on an hourly scale. While we recognize that wind conditions may vary slightly among
 462 different regimes, we argue that a spatial window of ± 15 km around the IASI centroids and a

463 temporal window ± 60 min around the overpass times were internally consistent with one another
464 and can be used to account for the transport of NH_3 under typical atmospheric conditions during
465 this period.

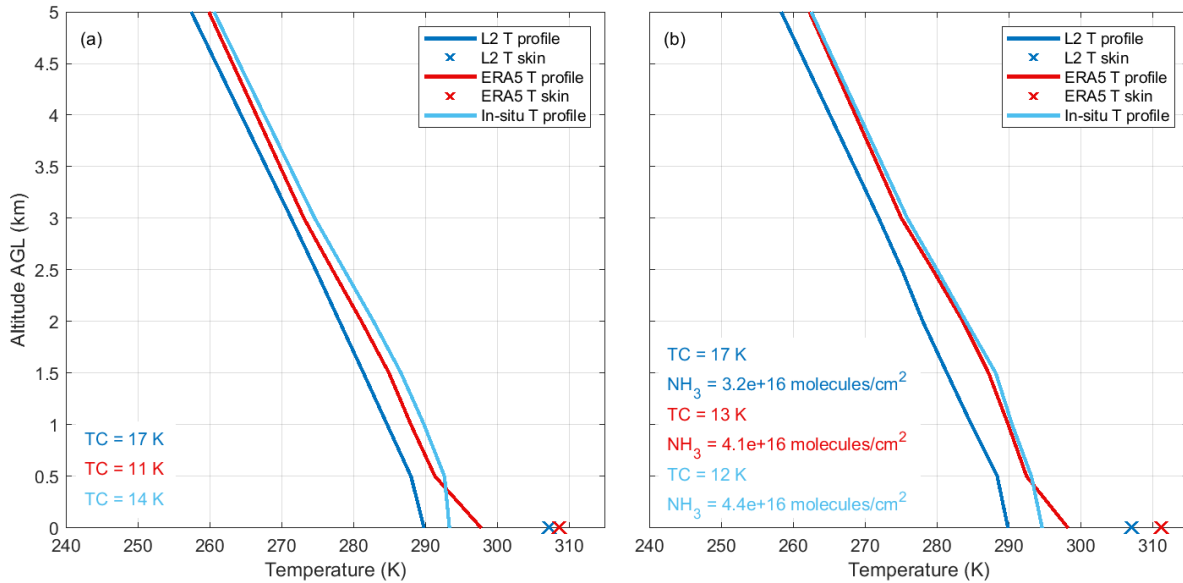
466 The near real-time product comparing with in-situ columns integrated up to the MLH and
467 within the ± 15 km and ± 60 min spatiotemporal window yielded a correlation coefficient of 0.58,
468 an intercept of $2.1 \pm 1.5 \times 10^{15}$ molec cm^{-2} and a slope of 0.78 ± 0.14 . The reanalysis product
469 showed no real changes in the correlation coefficient (0.57) and intercept ($1.3 \pm 1.9 \times 10^{15}$ molec
470 cm^{-2}), but a slope closer to unity (1.0 ± 0.19) was observed. The in-situ derived IASI product
471 showed a similar correlation (0.54), slope (1.1) and intercept ($1.7 \pm 2.2 \times 10^{15}$ molec cm^{-2}). All the
472 correlations are statistically significant. The intercepts for the three products are nearly
473 indistinguishable from zero, particularly when compared to column amounts $> 10^{16}$ molec cm^{-2} ,
474 suggesting that there is no significant absolute bias between the IASI and in-situ datasets.

475 Accurate temperature measurements are needed for NH_3 retrievals, especially in the
476 lower layers of the atmosphere where errors in the temperature profile can affect the retrieved
477 NH_3 columns significantly. The reanalysis product relies on gridded ECMWF meteorological
478 data, and our results showed the robustness of this implementation, which allows for long-term
479 consistent time series of IASI. The in-situ derived IASI product shows a slightly deviated slope
480 from unity, but the fact that this product matched well with the reanalysis product (Fig. 6d)
481 suggests that the retrievals are still internally coherent. The deviation may be attributed to the
482 fact that the in-situ temperature profiles largely consisted of sonde data, and sonde measurements
483 were not always representative of the IASI pixel in space and time. Our results are also
484 consistent with previous findings that the historic near real-time product (before the May 4, 2016
485 and the release of the IASI L2 version 6.2 by EUMETSAT) has a low bias against the reanalysis
486 product in version 2.1 of IASI NH_3 due an underestimation of the thermal contrasts between the
487 surface and the air at the altitude of interest (Van Damme *et al.*, 2017). The differences in
488 temperature inputs are further illustrated in Figure 7, where we plot the mean temperature profile
489 used in the retrieval of each IASI product (left panel) and an example of a single observation
490 (right panel). The different profile shapes and thermal contrast values explain why the retrieved
491 column abundances vary. The largest thermal contrast (TC, shown as inset) between the surface
492 temperature and skin temperature is found in the near real-time product, confirming the reason
493 why the retrieved columns are biased low against the other two products.



494

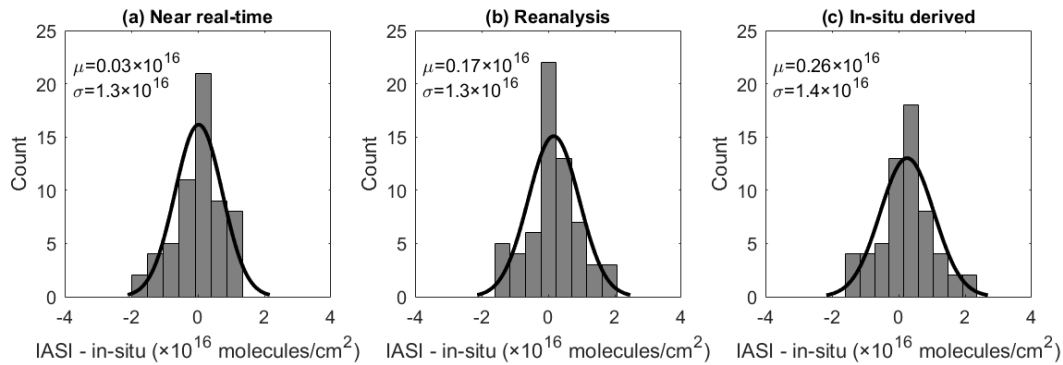
495 **Figure 6.** IASI-NH₃ products (a. near real-time, b. reanalysis, c. in-situ derived) versus the in-
 496 situ NH₃ columns in Colorado based on the ±15 km and ±60 min window and MLH assumption.
 497 The intracomparison between the reanalysis and in-situ derived IASI products is shown in (d).
 498 Red line shows the best fit using orthogonal regression. Dashed line represents the 1:1 slope.



499

500 **Figure 7.** EUMETSAT L2 (dark blue), ERA5 (red) and in situ (light blue) temperature profiles
 501 used in the retrieval of near real-time, reanalysis and custom IASI products. Left panel: mean
 502 temperature profile in this study; right panel: a single observation on Aug 3, 2014 from IASI
 503 Metop-A (39.867° N, 105.205° W).

504 While linear regression provides a straightforward picture of how two datasets match
 505 with each other, the fitted slopes and intercepts can be driven by outliers on either side. We
 506 additionally calculated histograms to check for potential differences that may exist between the
 507 IASI and in-situ measurements. The remainders obtained from subtracting in-situ columns from
 508 corresponding IASI columns are illustrated in Figure 8 (same scenarios as Fig. 6: IASI products
 509 versus the in-situ MLH assumption for the ± 15 km and ± 60 min window in Colorado). The
 510 Freedman-Diaconis rule was used to calculate the appropriate bin width and number of bins for
 511 each distribution (Freedman & Diaconis, 1981). A Gaussian function was used to fit the
 512 remainders for a smoother interpretation of distribution. The histograms show that the
 513 remainders were clustered around zero for all three products, with the near real-time product
 514 having the smallest mean. This again indicates that the IASI products do not appear to have large
 515 systematic biases. Therefore, averaging IASI observations under different scenarios
 516 (low/moderate/high NH_3) likely will yield improved detection limits as any random
 517 measurement noise become averaged out.



518

519 **Figure 8.** Histograms showing the remainders between IASI and in-situ NH_3 columns in
 520 Colorado (± 15 km, ± 60 min window, MLH assumption) for (a) the near real-time, (b) the
 521 reanalysis and (c) the in-situ derived products. The fitted Gaussian distribution is plotted as a
 522 black curve. μ and σ denote the mean and standard deviation of the fitted Gaussian function,
 523 respectively.

524 3.3. Comparison between Colorado and California

525 The DISCOVER-AQ California campaign was conducted over the San Joaquin Valley,
 526 the most productive agricultural region in the U.S., with Kern County and Tulare County ranking
 527 top in total value of production as of 2017 (CDFA, 2018). Previous studies have found
 528 significantly high NH_3 abundances in the San Joaquin Valley (Clarisse *et al.*, 2010; Makar *et al.*,
 529 2009), making it a good area to evaluate the sensitivity of IASI towards surface NH_3 . However,
 530 using the same criteria as for Colorado, only a limited number of collocated case ($N=3, 9, 4$ for
 531 near real-time, reanalysis and in-situ derived products) were found in California. Part of the
 532 reason was that only the Metop-A satellite was available during that time, whereas both MetOop-
 533 A and B were operational during the Colorado campaign. The main factor, however, was that the
 534 California campaign happened during winter in a valley area, where high cloud coverage, low
 535 thermal contrast and strong but shallow temperature inversions were frequently present. These
 536 conditions pose a challenge for accurate satellite NH_3 retrievals from an infrared sounder. For
 537 demonstration purposes, a test was conducted from January 16 to February 7, 2013 to retrieve
 538 NH_3 columns for all IASI Metop-A pixels within the DISCOVER-AQ California domain. Using
 539 the near real-time product as an example, only 23% of pixels produced valid columns after cloud
 540 filtering ($< 25\%$), and another 14% were removed after accounting for the availability of skin
 541 temperature and applying post-filtering, a process that is used to remove erroneous retrievals
 542 (Van Damme *et al.*, 2017). In contrast, a similar test between July 17 and August 10, 2014 over
 543 the DISCOVER-AQ Colorado domain showed that 52% of the Metop-A and B pixels remained
 544 after the retrieval process. The limited sample size makes it extremely difficult to draw any
 545 conclusions on the agreement between IASI and in-situ measurements in California. Given this,
 546 the scope of this study is limited to Colorado. The California example highlights the fact that
 547 validation results in one area may not apply to another area, especially where the conditions are
 548 dramatically different for satellite observations. Indeed, the same location may have different
 549 seasonality in the validation due to differences in thermal contrast. Similar to the results in
 550 Colorado, the reanalysis product in California yielded more datapoints available because of the
 551 increased availability of temperature profiles by using gridded, interpolated model data.

552 3.4. Comparison Between Spatiotemporal Windows

553 As described in section 3.2, we used the ± 15 km spatial window in conjunction with the
 554 ± 60 min temporal window to account for the transport of NH_3 based on the typical boundary
 555 layer wind speed of $3.5 \pm 2.2 \text{ m s}^{-1}$. We also evaluated the agreement between IASI and in-situ
 556 data using other combinations of spatiotemporal windows that may be relevant. For comparison
 557 purposes, we examined windows up to a factor of three apart in space and time to investigate the
 558 sensitivity of spatiotemporal windows on the outcomes. Table 3 lists the orthogonal regression
 559 results between IASI and the in-situ MLH assumption under nine different spatiotemporal
 560 windows. The near real-time IASI product is shown here as an example. The correlations in all
 561 nine windows are tested to be statistically significant. Aside from the ± 15 km and ± 60 min
 562 window that has been adopted throughout the analysis, the ± 15 km and ± 20 min window also
 563 showed good performance. The “within pixel” and ± 60 min window even outperforms the
 564 original window in terms of slope and correlation, which is reasonable since we anticipate that
 565 most NH_3 emitted will stay near their sources in a short time frame. However, it should be noted
 566 that the ± 15 km and ± 60 min window has a much larger sample size than the two windows
 567 above, providing higher statistical power. From a statistical perspective, none of the remaining
 568 windows are comparable to the ones discussed in terms of overall agreement.

569 **Table 3.** Orthogonal regression statistics between the near real-time IASI product and the in-situ
 570 MLH assumption for all the spatiotemporal windows tested, including overlapping points

Temporal window	20 min			60 min			180 min		
Spatial window	Within pixel	15 km	45 km	Within pixel	15 km	45 km	Within pixel	15 km	45 km
m	0.93 ± 0.17	0.76 ± 0.18	0.60 ± 0.17	2.1 ± 0.73	0.78 ± 0.14	0.85 ± 0.13	2.3 ± 0.50	2.7 ± 0.67	1.1 ± 0.15
b	8.0×10^{14} $\pm 2.4 \times 10^{15}$	1.2×10^{15} $\pm 2.7 \times 10^{15}$	3.4×10^{15} $\pm 1.5 \times 10^{15}$	-4.6×10^{15} $\pm 5.1 \times 10^{15}$	2.1×10^{15} $\pm 1.5 \times 10^{15}$	1.3×10^{15} $\pm 1.0 \times 10^{15}$	-3.9×10^{15} $\pm 3.2 \times 10^{15}$	-7.9×10^{15} $\pm 4.4 \times 10^{15}$	6.2×10^{14} $\pm 9.2 \times 10^{14}$
r	0.84	0.68	0.28	0.50	0.58	0.38	0.64	0.41	0.41
N	12	22	150	25	60	245	32	81	258
IASI mean	1.1×10^{16} $\pm 9.7 \times 10^{15}$	1.1×10^{16} $\pm 9.2 \times 10^{15}$	8.3×10^{15} $\pm 6.9 \times 10^{15}$	9.2×10^{15} $\pm 7.6 \times 10^{15}$	8.8×10^{15} $\pm 7.1 \times 10^{15}$	7.1×10^{15} $\pm 6.4 \times 10^{15}$	9.4×10^{15} $\pm 7.8 \times 10^{15}$	9.2×10^{15} $\pm 8.0 \times 10^{15}$	6.6×10^{15} $\pm 5.7 \times 10^{15}$
In-situ mean	1.1×10^{16} $\pm 1.0 \times 10^{16}$	1.3×10^{16} $\pm 1.1 \times 10^{16}$	8.1×10^{15} $\pm 8.0 \times 10^{15}$	6.6×10^{15} $\pm 5.1 \times 10^{15}$	8.5×10^{15} $\pm 8.2 \times 10^{15}$	6.8×10^{15} $\pm 6.8 \times 10^{15}$	5.7×10^{15} $\pm 4.4 \times 10^{15}$	6.3×10^{15} $\pm 5.0 \times 10^{15}$	5.5×10^{15} $\pm 5.5 \times 10^{15}$

571 *Note.* “Within pixel” means that the in-situ measurements must be located within the actual IASI
 572 pixel (~ 12 km in diameter). m = slope; b = y-intercept (x-axis = in-situ, y-axis = IASI); r =
 573 Pearson’s correlation coefficient; N = number of datapoints. Standard deviations are shown for
 574 slopes, intercepts and means.

575 3.5. Ascent and Descent Aircraft Profiles

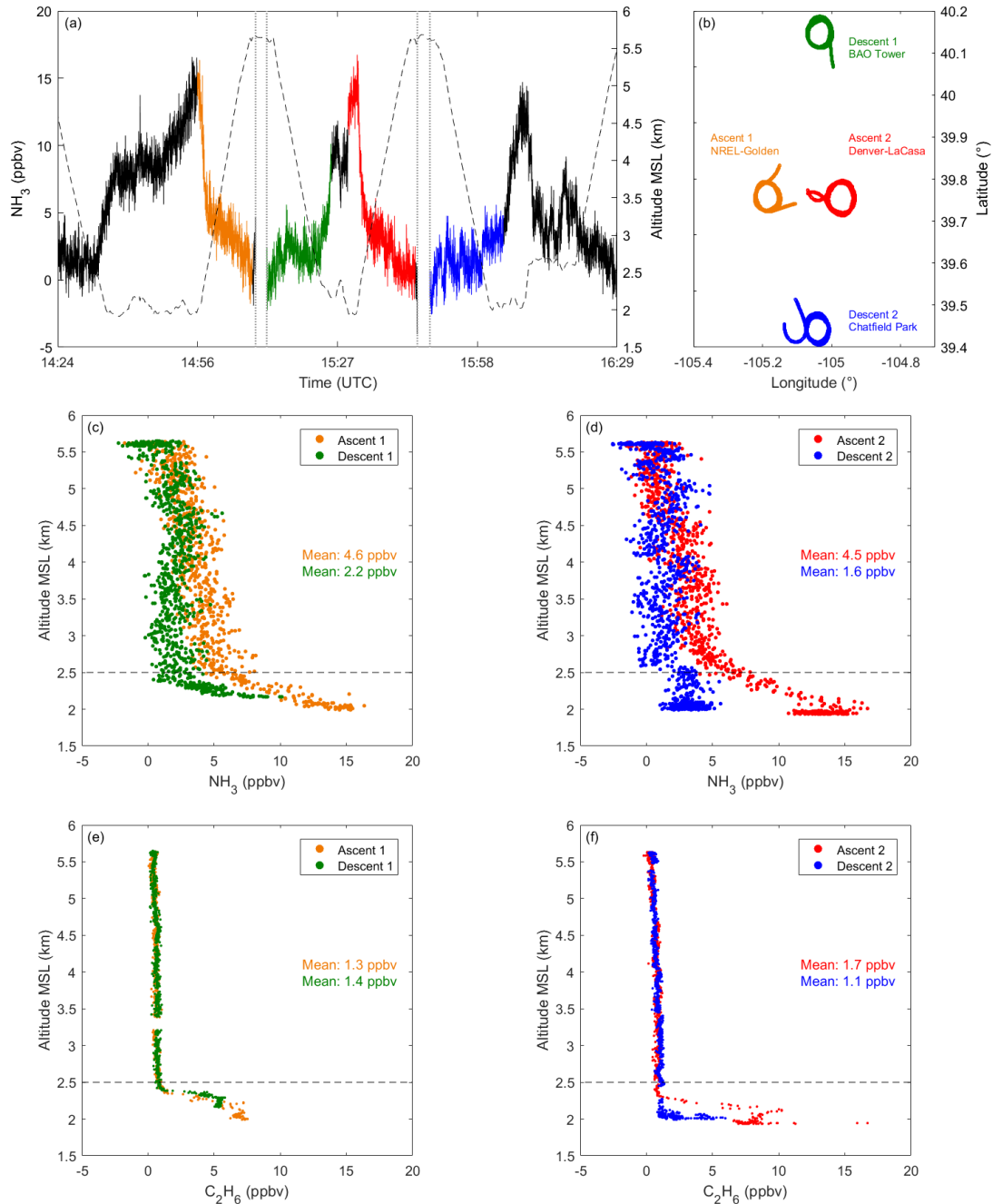
576 An earlier study on the validation of TES NH_3 suggested that the two airborne NH_3
 577 sensors (PTR-MS and CRDS) in DISCOVER-AQ California exhibited hysteresis during
 578 sampling (Sun *et al.*, 2015). Due to the sensors’ relatively long response times, the measured

579 NH_3 concentrations showed long tails of decay when exiting the boundary layer into the free
580 troposphere. On the other hand, the sensors detected almost no NH_3 signals when descending
581 from the free troposphere until reaching the boundary layer, likely due to an extended portion of
582 outgassing in clean conditions prior to the descent. The Colorado campaign only had PTR-MS
583 onboard the P-3B aircraft, but we also examined the differences in validation using the ascent
584 and descent profiles. It is emphasized that NH_3 data were only a side product of the PTR-MS
585 measurements during DISCOVER-AQ. The instrument was primarily measuring volatile organic
586 compounds (VOCs) and thus not optimized for detecting NH_3 (high instrumental background
587 resulting in a poor detection limit, slow time response due to a ~2 m long inlet line).

588 As an example of the hysteresis in sampling, we selected two pairs of locations relatively
589 close to each other where aircraft profiling was conducted to minimize the influence of NH_3
590 gradients across the transect. Figure 9a shows the time series on July 23, 2014, of NH_3 for an
591 ascent profile at NREL (Golden), a high-altitude leg near 5.5 km MSL for 22 km (2.5 min) and
592 then a descent spiral profile near the BAO tower (near Erie). The second pair of profiles
593 consisted of an ascent at Denver (La Casa), another high-altitude segment at 5.5 km MSL for 26
594 km (3 min.), followed by a descent at Chatfield Park south of Denver. MLH was estimated from
595 the aircraft temperature profiles and found to be similar between these locations (difference
596 within 100 m). The geographical locations of the four sites are shown in Figure 9b.

597 Figure 9c and d show the vertical profiles of NH_3 for the near-adjacent ascent and descent
598 pairs. For comparison, Figure 9e and f show the same pairs of profiles for C_2H_6 , a petrochemical
599 tracer with a ~ 2 month lifetime that has sources located in the same general areas as NH_3
600 emissions in northeast Colorado and has no sampling issues (Kille *et al.*, 2019). The dashed line
601 marks the average boundary layer height averaged between each pair. For the first set of profiles
602 (Fig. 9c), the descent had an average NH_3 mixing ratio of 2.2 ppbv while the ascent averaged
603 over two times higher at 4.6 ppbv. We hypothesize these differences were mainly due to
604 instrument sampling issues because the corresponding C_2H_6 profiles (Fig. 9e) showed no
605 noticeable differences between the two sites, particularly the relative shapes of the profiles
606 around the MLH. This sampling hysteresis for NH_3 is consistent with those reported by Sun *et al.*
607 (2015). We investigated several other profiles and found similar patterns, especially when there
608 were large enhancements of NH_3 (> 5 ppbv) near the ground, suggesting that PTR-MS was
609 subject to artifacts caused by instrument design and sampling method as expected for any inlet-
610 based instrument.

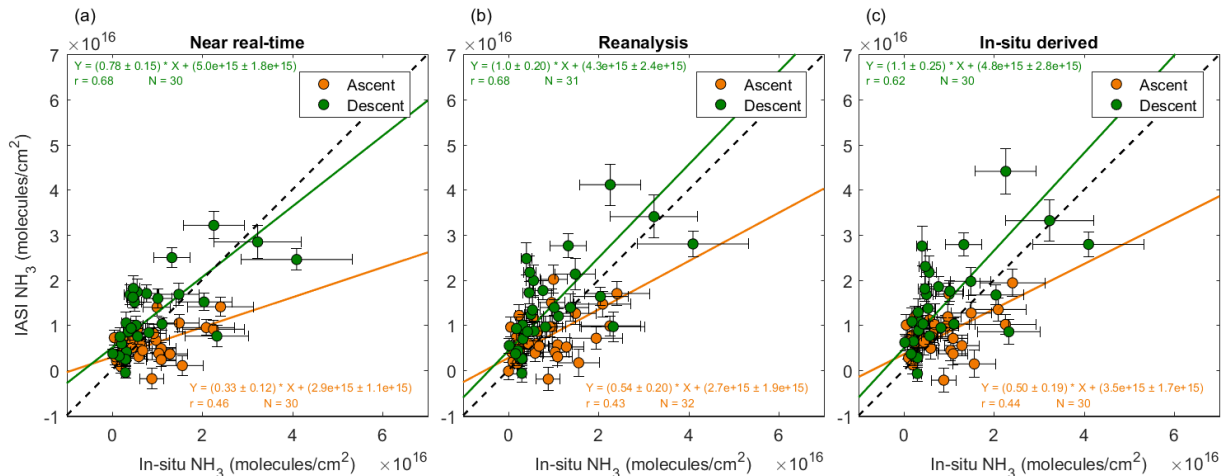
611 For the second pair (Fig. 9d), the average NH_3 during descent again was lower than the
612 ascent, but there was a difference in air mass between these two sites. Figure 9f shows that C_2H_6
613 had different boundary layer profiles in the two locations, though were indistinguishable at and
614 above it. Nonetheless, the relative shapes of the NH_3 and C_2H_6 profiles are dramatically
615 different, with C_2H_6 showing an abrupt and large decrease above the MLH while NH_3 shows a
616 more gradual decrease around the MLH. The more gradual transition of NH_3 is again likely
617 related to sampling biases, though real air mass differences certainly play some role at least in
618 the boundary layer.



619

620 **Figure 9.** Vertical profiles of 1 Hz NH_3 and C_2H_6 measurements on the P-3B in Colorado on
 621 July 23, 2014. Panel (a) shows the time series of NH_3 measured by the PTR-MS. The two pairs
 622 of adjacent ascent and descent profiles selected for comparison are highlighted by different
 623 colors. The thin dashed line and grey dotted vertical lines show the altitude change during the
 624 flight and breaks in the time series, respectively. Panel (b) shows the geographical locations
 625 where the aircraft profiles were made. Panels (c) and (d) present the NH_3 profiles during the
 626 ascents and descents. Dashed lines mark the MLH averaged across each ascent and descent pair.
 627 Panels (e) and (f) are the corresponding C_2H_6 profiles measured simultaneously by a TILDAS
 628 instrument.

629 While we have demonstrated that IASI is comparable to in-situ-derived profiles in
 630 general, the differences between ascent and descent profiles due to sampling issues require more
 631 examination. To distinguish between ascent and descent aircraft profiles, we now compare the
 632 three IASI products against ascents and descents separately (Fig. 10), and key differences are
 633 readily observed. For example, the ascent profiles yield higher columns than corresponding IASI
 634 columns, consistent with the above observations of instrument artifacts from outgassing.
 635 Likewise, descent profiles are generally lower due to surface adsorption upon rapid increases in
 636 NH_3 concentrations as one descends. As a result, descent clusters have higher slopes than the
 637 ascent clusters. Descents tend to have much better correlations than ascents (0.62-0.68 vs. 0.43-
 638 0.46) as well as slopes closer to unity, but their intercepts also tend to be worse. Because
 639 sampling biases occur after large concentration changes regardless of the direction (net
 640 adsorption vs. net outgassing), it is unclear which of these profiles is more representative of the
 641 actual distribution. Therefore, we have opted to aggregate all PTR-MS measurements together
 642 regardless of the flight direction. Our findings suggest that attention needs to be paid to the
 643 discrepancies between ascent and descent profiles as a metric of in-situ, instrument
 644 inlet/sampling performance. Future airborne research campaign targeting NH_3 concentrations
 645 should employ sensors with highly quantified instrument responses in-flight, during upward and
 646 downward flight profiles in the same location, and with high precisions and low biases for better
 647 mapping of NH_3 vertical profiles.

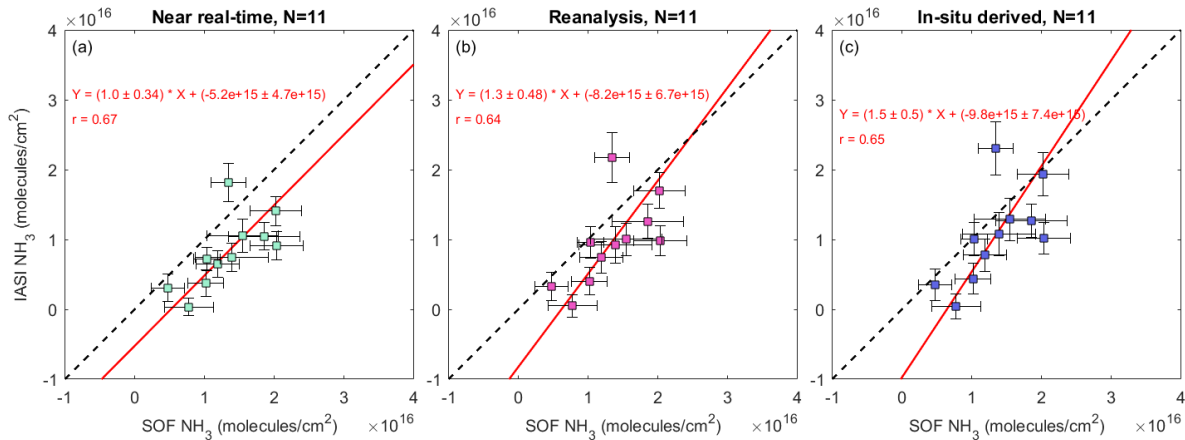


648
 649 **Figure 10.** IASI- NH_3 products versus the in-situ NH_3 columns in Colorado (± 15 km and ± 60
 650 min window and MLH assumption) with ascent (orange) and descent (green) aircraft profiles
 651 analyzed separately (same data as in Figure 6).

652 3.6. Comparison between IASI and CU SOF

653 Aside from in-situ NH_3 concentrations, ground-based mobile CU-SOF measurements of
 654 NH_3 total columns were also available during the DISCOVER-AQ/FRAPPÉ Colorado campaign
 655 (Kille *et al.*, 2017). We filtered the FTIR data using the same algorithm as the other in-situ
 656 platforms but enlarged the window to ± 15 km and ± 180 min to include additional data that may
 657 be potentially relevant. This was based on the variability of wind speed measured at BAO
 658 (3.5 ± 2.2 m s⁻¹), where the ± 15 km and ± 180 min window is consistent with the lower boundary

659 of wind speed at 1σ standard deviation (1.3 m s^{-1}). For each collocation, the mean of all CU SOF
 660 data within the window was computed. Figure 11 shows that IASI has moderate correlations
 661 with FTIR, and the slopes are consistent with the 1:1 line. Given that FTIR retrievals depend
 662 only weakly on a priori parameters ($< 4\%$ variation in column sensitivities), which also come
 663 with large uncertainties (Kille *et al.*, 2019), this comparison shows some promising consistency
 664 between the two instruments and independent approaches.



665

666 **Figure 11.** IASI versus CU SOF NH_3 columns using orthogonal regression for (a) the near real-
 667 time, (b) the reanalysis, and (c) the in-situ derived products within the $\pm 15 \text{ km}$ and $\pm 180 \text{ min}$
 668 window in Colorado. All the correlations are statistically significant.

669 4. Implications

670 In the past decade, satellite NH_3 measurements have been used to study the trends and
 671 distributions of NH_3 owing to their long data record and global coverage (Dammers *et al.*, 2019;
 672 Pinder *et al.*, 2011; Van Damme *et al.*, 2018; Warner *et al.*, 2016). Although research has
 673 attempted to validate satellite NH_3 using surface concentrations and ground-based stationary
 674 FTIR measurements, the accuracies of localized measurements - which are important for
 675 studying emission sources and their variabilities - have not been thoroughly validated. In this
 676 work, we compared IASI with collocated in-situ-derived profiles and mobile SOF columns from
 677 a suite of aircraft, tower, mobile laboratory, and sonde measurements from the NASA
 678 DISCOVER-AQ and NSF FRAPPÉ field experiments. We validated version 3 of the IASI NH_3
 679 dataset with three temperature profiles: the near real-time product from EUMETSAT, the
 680 ERA5/ECMWF reanalysis product, and one using in-situ temperature profiles from the
 681 DISCOVER-AQ/FRAPPÉ campaign.

682 IASI correlates well with in-situ NH_3 integrated up to the MLH within windows of ± 15
 683 km from the IASI centroid and $\pm 60 \text{ min}$ of the overpass time. The three IASI products show
 684 similar performances, with the reanalysis product showing the overall best agreement (slope =
 685 1.0 ± 0.19 , intercept = $(1.3 \pm 1.9) \times 10^{15} \text{ molec cm}^{-2}$, $r = 0.57$). Because IASI has no significant
 686 biases compared to the in-situ profiles, IASI columns can be spatiotemporally averaged for
 687 improved signal to noise ratios where appropriate. The IASI retrieval depends on accurate
 688 temperature inputs, especially in the boundary layer where most NH_3 resides. The near-real time

689 product showed a slight bias in the slope, which could be readily traced back to a known bias in
690 the IASI L2 temperature profile prior to 2016. Newer data do not exhibit such biases, with near-
691 real time and reanalysis products agreeing in the mean (Van Damme *et al.*, 2017). Limited
692 mobile CU SOF measurements during DISCOVER-AQ/FRAPPÉ Colorado also show overall
693 good consistency with IASI. Our IASI results are demonstrated for summer in Colorado USA
694 but may not be representative of other locations and times. More validations are needed,
695 especially in cases with strong inversions and low thermal contrast such as in valleys and in
696 winter. Large columns ($> 5 \times 10^{16}$ molec cm⁻²) could also not be validated with the current set of
697 in situ measurements. We remind here that no AVK information was generated from IASI
698 retrievals or applied to the in-situ data, and therefore this study only presents a comparison
699 between the unbiased IASI columns and in-situ integrated columns. A weighting function is
700 being considered for future IASI versions that can be used to account for the variabilities of
701 vertical sensitivity.

702 This study is the first validation of IASI NH₃ at the single pixel scale using vertically
703 integrated in-situ concentrations. Nonetheless, as with TES single pixel validation results,
704 sampling artifacts of airborne NH₃ instruments remain a significant barrier for improved
705 validations. Not only are there fewer measurements of free tropospheric NH₃ from airborne
706 science field campaigns compared to other in-situ trace gases, but high accuracy and fast
707 response NH₃ measurements are critically needed for the mapping of NH₃ vertical profiles. This
708 is particularly important for validating in source regions where elevated concentrations in the
709 boundary layer may influence the corresponding free tropospheric values due to sampling biases
710 of existing instruments. Besides, vertical profiles of NH₃ in the boundary layer themselves have
711 complex structures due to emissions, partitioning into aerosol phases, and temperature and
712 relative humidity changes. More boundary layer NH₃ profiles will improve the development of
713 retrieval algorithms for all infrared sounders, and this can be achieved with recent advances in
714 NH₃ measurements techniques and the increased availability of airborne research campaigns
715 (Miller *et al.*, 2014; Pollack *et al.*, 2019).

716 Vertical profiles of NH₃ in the free troposphere are also a high priority, as the integrated
717 NH₃ concentrations in the free troposphere may be comparable to the overall column abundance
718 in low and moderate NH₃ locations. Spiral, vertical aircraft profiles like those made in
719 DISCOVER-AQ are critical for the validation of short-lived species like NH₃ such that
720 horizontal gradients are not manifested as vertical gradients during altitude changes. In addition,
721 repeated upward and downward transects over the same airmass will provide a measure of
722 confidence in any potential instrument sampling biases. While our study focuses on the
723 measurements from IASI, these generalized conclusions hold for all infrared sounders that are
724 sensitive to boundary layer temperature profiles and thermal contrast. Overall, more robust
725 datasets are needed for validating satellite NH₃ measurements, particularly at the pixel scale as
726 satellite NH₃ datasets are applied toward higher-resolution emission inventories and atmospheric
727 composition analyses.

728 **Acknowledgments**

729 Xuehui Guo gratefully acknowledges the NASA Earth and Space Science Fellowship
730 (Grant number: 80NSSC17K0377) for funding the work. We also gratefully acknowledge
731 support for the analyses of the IASI and in-situ data products from the NASA Health and Air

732 Quality Applied Sciences (HAQAST) team, NASA NNX16AQ90G. Mark A. Zondlo
733 acknowledges support as a visiting scientist at ULB from the EUMETSAT Satellite Application
734 Facility on Atmospheric Chemistry Monitoring (AC SAF). Princeton field data collection and
735 data quality control in Colorado/California by Levi Golston and Da Pan were supported by
736 NASA NNX14AT36G and NNX14AT32G. We acknowledge Lars Wendt, Victor Fu, Naomi
737 Pohl, and Levi Stanton for their assistance with the Princeton field data collection in Colorado
738 and California. Part of the research at the ULB has been supported by the IASI.Flow Prodex
739 arrangement (ESA--BELSPO). Lieven Clarisse and Martin Van Damme are respectively a
740 research associate and a postdoctoral researcher supported by the F.R.S.-FNRS. Cathy Clerbaux
741 is grateful to CNES and Centre National de la Recherche Scientifique (CNRS) for financial
742 support. IASI is a joint mission of EUMETSAT and the Centre National d'Etudes Spatiales
743 (CNES, France). The IASI Level-1C data are distributed in near real-time by EUMETSAT
744 through the EUMETCast distribution system. We acknowledge the AERIS data infrastructure
745 <https://www.aeris-data.fr> for providing access to the IASI data as well as the NASA
746 DISCOVER-AQ and NSF FRAPPÉ science teams, aircraft and technical crews. PTR-MS
747 measurements during DISCOVER-AQ were supported by the Austrian Federal Ministry for
748 Transport, Innovation and Technology (bmvit) through the Austrian Space Applications
749 Programme (ASAP 8, #833451, #840086) of the Austrian Research Promotion Agency (FFG).
750 Tomas Mikoviny was supported by an appointment to the NASA Postdoctoral Program at the
751 Langley Research Center administered by Oak Ridge Associated Universities (ORAU) under
752 contract with NASA. iMet-1 temperature soundings were provided by Anne Thompson
753 (NASA/Goddard) and her Penn State students supported by NASA NNX10AR39G and
754 NNX11AQ44G. UW-Madison SSEC RS92 temperature measurements were conducted by Erik
755 Olson. The NO₂ data on P-3B were made available by Andrew J. Weinheimer and Denise D.
756 Montzka. The number concentrations of particles were measured by Bruce E. Anderson. The
757 HSRL2 MLH measurements on B200 were made by Amy Jo Scarino, Chris A. Hostetler,
758 Richard A. Ferrare and Sharon P. Burton. Rainer Volkamer acknowledges financial support for
759 the CU SOF deployment during FRAPPÉ from the Colorado Department for Public Health and
760 Environment (CDPHE) State of Colorado contract 14FAA64390, and US National Science
761 Foundation (NSF) EAGER grant AGS-1452317. N.K. and Rainer Volkamer acknowledges S.
762 Baidar, R. Sinreich, I. Ortega, P. Handley, O.W. Cooper for help during the field campaign, and
763 J. Hannigan for access to the NCAR trailer. We also thank Cody Floerchinger and Scott C.
764 Herndon for their contributions to the Aerodyne mobile lab measurements.

765

766 **Data Availability**

767 All the datasets used in this work are publicly available and archived at the following websites:

768 DISCOVER-AQ/FRAPPÉ: <https://www-air.larc.nasa.gov/missions/discover-aq/discover-aq.html>

769 IASI: <https://iasi.aeris-data.fr/NH3/>

770

771 **References**

772 Baidar, S., Kille, N., Ortega, I., Sinreich, R., Thomson, D., Hannigan, J., & Volkamer, R. (2016).
773 Development of a digital mobile solar tracker. *Atmospheric Measurement Techniques*, 9(3),

- 774 963–972. <https://doi.org/10.5194/amt-9-963-2016>
- 775 Behera, S. N., Sharma, M., Aneja, V. P., & Balasubramanian, R. (2013). Ammonia in the
776 atmosphere: A review on emission sources, atmospheric chemistry and deposition on
777 terrestrial bodies. *Environmental Science and Pollution Research*, 20(11), 8092–8131.
778 <https://doi.org/10.1007/s11356-013-2051-9>
- 779 Beusen, A. H. W., Bouwman, A. F., Heuberger, P. S. C., Van Drecht, G., & Van Der Hoek, K.
780 W. (2008). Bottom-up uncertainty estimates of global ammonia emissions from global
781 agricultural production systems. *Atmospheric Environment*, 42(24), 6067–6077.
782 <https://doi.org/10.1016/j.atmosenv.2008.03.044>
- 783 Beyersdorf, A. J., Ziemba, L. D., Chen, G., Corr, C. A., Crawford, J. H., Diskin, G. S., ...
784 Anderson, B. E. (2016). The impacts of aerosol loading, composition, and water uptake on
785 aerosol extinction variability in the Baltimore-Washington, D.C. region. *Atmospheric
786 Chemistry and Physics*, 16(2), 1003–1015. <https://doi.org/10.5194/acp-16-1003-2016>
- 787 Bouwman, A. F., Lee, D. S., Asman, W. A. H., Dentener, F. J., Hoek, K. W. Van Der, Olivier, J.
788 G. J., & Tg, N. (1997). A global high-resolution emission inventory for ammonia. *Global
789 Biogeochemical Cycles*, 11(4), 561–587.
- 790 CDFA. (2018). *California Agricultural Statistics Review 2017-2018*. Retrieved from
791 www.cdfa.ca.gov/statistics
- 792 Clarisse, L., Clerbaux, C., Dentener, F., Hurtmans, D., & Coheur, P.-F. (2009). Global ammonia
793 distribution derived from infrared satellite observations. *Nature Geoscience*, 2(7), 479–483.
794 <https://doi.org/10.1038/ngeo551>
- 795 Clarisse, L., Shephard, M. W., Dentener, F., Hurtmans, D., Cady-Pereira, K., Karagulian, F., ...
796 Coheur, P. F. (2010). Satellite monitoring of ammonia: A case study of the San Joaquin
797 Valley. *Journal of Geophysical Research Atmospheres*, 115(13), 1–15.
798 <https://doi.org/10.1029/2009JD013291>
- 799 Clerbaux, C., Boynard, A., Clarisse, L., George, M., Hadji-Lazaro, J., Herbin, H., ... Coheur, P.-
800 F. (2009). Monitoring of atmospheric composition using the thermal infrared IASI/MetOp
801 sounder. *Atmospheric Chemistry and Physics*, 9(16), 6041–6054.
802 <https://doi.org/10.5194/acp-9-6041-2009>
- 803 Coheur, P. F., Clarisse, L., Turquety, S., Hurtmans, D., & Clerbaux, C. (2009). IASI
804 measurements of reactive trace species in biomass burning plumes. *Atmospheric Chemistry
805 and Physics*, 9(15), 5655–5667. <https://doi.org/10.5194/acp-9-5655-2009>
- 806 Crawford, J. H., & Pickering, K. E. (2014). DISCOVER-AQ: Advancing Strategies for Air
807 Quality Observations in the Next Decade. *Air & Waste Management Association*, 1–47.
808 Retrieved from <https://www.awma.org/content.asp?admin=Y&contentid=301>
- 809 Dammers, E., McLinden, C. A., Griffin, D., Shephard, M. W., Van Der Graaf, S., Lutsch, E., ...
810 Erisman, J. W. (2019). NH₃ emissions from large point sources derived from CrIS and IASI
811 satellite observations. *Atmospheric Chemistry and Physics*, 19(19), 12261–12293.
812 <https://doi.org/10.5194/acp-19-12261-2019>
- 813 Dammers, E., Palm, M., Van Damme, M., Vigouroux, C., Smale, D., Conway, S., ... Erisman, J.
814 W. (2016). An evaluation of IASI-NH₃ with ground-based Fourier transform infrared

- 815 spectroscopy measurements. *Atmos. Chem. Phys.*, *16*, 10351–10368.
816 <https://doi.org/10.5194/acp-16-10351-2016>
- 817 Dammers, E., Shephard, M. W., Palm, M., Cady-Pereira, K., Capps, S., Lutsch, E., ... Willem
818 Erisman, J. (2017). Validation of the CrIS fast physical NH₃ retrieval with ground-based
819 FTIR. *Atmospheric Measurement Techniques*, *10*(7), 2645–2667.
820 <https://doi.org/10.5194/amt-10-2645-2017>
- 821 Dammers, E., Vigouroux, C., Palm, M., Mahieu, E., Warneke, T., Smale, D., ... Erisman, J. W.
822 (2015). Retrieval of ammonia from ground-based FTIR solar spectra. *Atmospheric*
823 *Chemistry and Physics Discussions*, *15*(16), 23279–23315. [https://doi.org/10.5194/acpd-15-](https://doi.org/10.5194/acpd-15-23279-2015)
824 [23279-2015](https://doi.org/10.5194/acpd-15-23279-2015)
- 825 Dentener, F. J., & Crutzen, P. J. (1994). A three-dimensional model of the global ammonia cycle.
826 *Journal of Atmospheric Chemistry*, *19*(4), 331–369. <https://doi.org/10.1007/BF00694492>
- 827 Eilerman, S. J., Peischl, J., Neuman, J. A., Ryerson, T. B., Aikin, K. C., Holloway, M. W., ...
828 Herndon, S. (2016). Characterization of Ammonia, Methane, and Nitrous Oxide Emissions
829 from Concentrated Animal Feeding Operations in Northeastern Colorado. *Environmental*
830 *Science and Technology*, *50*(20), 10885–10893. <https://doi.org/10.1021/acs.est.6b02851>
- 831 Ellis, R. A., Murphy, J. G., Pattey, E., Van Haarlem, R., O'Brien, J. M., & Herndon, S. C.
832 (2010). Characterizing a Quantum Cascade Tunable Infrared Laser Differential Absorption
833 Spectrometer (QC-TILDAS) for measurements of atmospheric ammonia. *Atmospheric*
834 *Measurement Techniques*, *3*(2), 397–406. <https://doi.org/10.5194/amt-3-397-2010>
- 835 Erisman, J. W., Sutton, M. A., Galloway, J., Klimont, Z., & Winiwarter, W. (2008). How a
836 century of ammonia synthesis changed the world. *Nature Geoscience*, *1*(10), 636–639.
837 <https://doi.org/10.1038/ngeo325>
- 838 Fehsenfeld, F. C., Huey, L. G., Leibrock, E., Dissly, R., Williams, E., Ryerson, T. B., ...
839 Hartsell, B. (2002). Results from an informal intercomparison of ammonia measurement
840 techniques. *Journal of Geophysical Research Atmospheres*, *107*(24), 1–15.
841 <https://doi.org/10.1029/2001JD001327>
- 842 Flocke, F., Pfister, G., Crawford, J. H., Pickering, K. E., Pierce, G., Bon, D., & Reddy, P. (2020).
843 Air Quality in the Northern Colorado Front Range Metro Area: The Front Range Air
844 Pollution and Photochemistry Experiment (FRAPPÉ). *Journal of Geophysical Research:*
845 *Atmospheres*, *125*(2). <https://doi.org/10.1029/2019JD031197>
- 846 Follette-Cook, M. B., Pickering, K. E., Crawford, J. H., Duncan, B. N., Loughner, C. P., Diskin,
847 G. S., ... Weinheimer, A. J. (2015). Spatial and temporal variability of trace gas columns
848 derived from WRF/Chem regional model output: Planning for geostationary observations of
849 atmospheric composition. *Atmospheric Environment*, *118*, 28–44.
850 <https://doi.org/10.1016/j.atmosenv.2015.07.024>
- 851 Fortems-Cheiney, A., Dufour, G., Hamaoui-Laguél, L., Foret, G., Siour, G., Van Damme, M., ...
852 Beekmann, M. (2016). Unaccounted variability in NH₃ agricultural sources detected by
853 IASI contributing to European spring haze episode. *Geophysical Research Letters*, *43*(10),
854 5475–5482. <https://doi.org/10.1002/2016GL069361>
- 855 Franco, B., Clarisse, L., Stavrou, T., Müller, J. F., Van Damme, M., Whitburn, S., ... Coheur,
856 P. F. (2018). A General Framework for Global Retrievals of Trace Gases From IASI:

- 857 Application to Methanol, Formic Acid, and PAN. *Journal of Geophysical Research:*
858 *Atmospheres*, 123(24), 13,963–13,984. <https://doi.org/10.1029/2018JD029633>
- 859 Freedman, D., & Diaconis, P. (1981). On the histogram as a density estimator:L2 theory.
860 *Zeitschrift Für Wahrscheinlichkeitstheorie Und Verwandte Gebiete*, 57(4), 453–476.
861 <https://doi.org/10.1007/BF01025868>
- 862 Galloway, J. N., Dentener, F. J., Capone, D. G., Boyer, E. W., Howarth, R. W., Seitzinger, S. P.,
863 ... Vöösmary, C. J. (2004). Nitrogen Cycles: Past, Present, and Future. *Biogeochemistry*,
864 70(2), 153–226. <https://doi.org/10.1007/s10533-004-0370-0>
- 865 Golston, L. M., Pan, D., Sun, K., Tao, L., Zondlo, M. A., Eilerman, S. J., ... Floerchinger, C.
866 (2020). Variability of ammonia and methane emissions from animal feeding operations in
867 northeastern Colorado. *Environmental Science and Technology*, es-2020-00301u.R1.
- 868 Herndon, S. C., Jayne, J. T., Zahniser, M. S., Worsnop, D. R., Knighton, B., Alwine, E., ... Kolb,
869 C. E. (2005). Characterization of urban pollutant emission fluxes and ambient concentration
870 distributions using a mobile laboratory with rapid response instrumentation. *Faraday*
871 *Discussions*, 130(0), 327–339. <https://doi.org/10.1039/B500411J>
- 872 Hoell, J. M., Harward, C. N., & Williams, B. S. (1980). Remote infrared heterodyne radiometer
873 measurements of atmospheric ammonia profiles. *Geophysical Research Letters*, 7(5), 313–
874 316.
- 875 Höpfner, M., Ungermann, J., Borrmann, S., Wagner, R., Spang, R., Riese, M., ... Wohltmann, I.
876 (2019). Ammonium nitrate particles formed in upper troposphere from ground ammonia
877 sources during Asian monsoons. *Nature Geoscience*, 12(8), 608–612.
878 <https://doi.org/10.1038/s41561-019-0385-8>
- 879 Höpfner, M., Volkamer, R., Grabowski, U., Grutter, M., Orphal, J., Stiller, G., ... Wetzel, G.
880 (2016). First detection of ammonia (NH₃) in the Asian summer monsoon upper
881 troposphere. *Atmospheric Chemistry and Physics*, 16(22), 14357–14369.
882 <https://doi.org/10.5194/acp-16-14357-2016>
- 883 IPCC. (2013). *Climate change 2013: The physical science basis, Intergovernmental Panel on*
884 *Climate Change (Ch. 8, p. 682)*. Cambridge, United Kingdom and New York, NY, USA:
885 Cambridge University Press.
- 886 Kille, N., Baidar, S., Handley, P., Ortega, I., Sinreich, R., Cooper, O. R., ... Volkamer, R.
887 (2017). The CU mobile Solar Occultation Flux instrument: Structure functions and emission
888 rates of NH₃, NO₂ and C₂H₆. *Atmospheric Measurement Techniques*, 10(1), 373–392.
889 <https://doi.org/10.5194/amt-10-373-2017>
- 890 Kille, N., Chiu, R., Frey, M., Hase, F., Sha, M. K., Blumenstock, T., ... Volkamer, R. (2019).
891 Separation of Methane Emissions From Agricultural and Natural Gas Sources in the
892 Colorado Front Range. *Geophysical Research Letters*, 46(7), 3990–3998.
893 <https://doi.org/10.1029/2019GL082132>
- 894 Lamarque, J. F., Kyle, P. P., Meinshausen, M., Riahi, K., Smith, S. J., van Vuuren, D. P., ... Vitt,
895 F. (2011). Global and regional evolution of short-lived radiatively-active gases and aerosols
896 in the Representative Concentration Pathways. *Climatic Change*, 109(1), 191–212.
897 <https://doi.org/10.1007/s10584-011-0155-0>

- 898 Li, Y., Schichtel, B. A., Walker, J. T., Schwede, D. B., Chen, X., Lehmann, C. M. B., ... Collett,
899 J. L. (2016). Increasing importance of deposition of reduced nitrogen in the United States.
900 *Proceedings of the National Academy of Sciences of the United States of America*, 113(21),
901 5874–5879. <https://doi.org/10.1073/pnas.1525736113>
- 902 Makar, P. A., Moran, M. D., Zheng, Q., Cousineau, S., Sassi, M., Duhamel, A., ... Bouchet, V.
903 S. (2009). Modelling the impacts of ammonia emissions reductions on North American air
904 quality. *Atmospheric Chemistry and Physics*, 9(18), 7183–7212.
905 <https://doi.org/10.5194/acp-9-7183-2009>
- 906 Mensink, C., & Deutsch, F. (2008). On the role of ammonia in the formation of PM_{2.5}. *NATO*
907 *Science for Peace and Security Series C: Environmental Security*, 548–556.
908 https://doi.org/10.1007/978-1-4020-8453-9_60
- 909 Miller, D. J., Sun, K., Tao, L., Khan, M. a., & Zondlo, M. a. (2014). Open-path, quantum
910 cascade-laser-based sensor for high-resolution atmospheric ammonia measurements.
911 *Atmospheric Measurement Techniques*, 7(1), 81–93. <https://doi.org/10.5194/amt-7-81-2014>
- 912 Miller, D. J., Sun, K., Tao, L., Zondlo, M. a., Nowak, J. B., Liu, Z., ... Scarino, A. J. (2015).
913 Ammonia and methane dairy emission plumes in the San Joaquin Valley of California from
914 individual feedlot to regional scales. *Journal of Geophysical Research: Atmospheres*, n/a-
915 n/a. <https://doi.org/10.1002/2015JD023241>
- 916 Mizak, C. A., Campbell, S. W., Luther, M. E., Carnahan, R. P., Murphy, R. J., & Poor, N. D.
917 (2005). Below-cloud ammonia scavenging in convective thunderstorms at a coastal research
918 site in Tampa, FL, USA. *Atmospheric Environment*, 39(9), 1575–1584.
919 <https://doi.org/10.1016/j.atmosenv.2004.10.008>
- 920 Müller, M., Mikoviny, T., Feil, S., Haidacher, S., Hanel, G., Hartungen, E., ... Wisthaler, A.
921 (2014). A compact PTR-ToF-MS instrument for airborne measurements of volatile organic
922 compounds at high spatiotemporal resolution. *Atmospheric Measurement Techniques*,
923 7(11), 3763–3772. <https://doi.org/10.5194/amt-7-3763-2014>
- 924 National Atmospheric Deposition Program. (2019). Ammonia Monitoring Network (AMoN).
925 Retrieved from <http://nadp.slh.wisc.edu/AMoN/>
- 926 Nemitz, E., Milford, C., & Sutton, M. A. (2001). A two-layer canopy compensation point model
927 for describing bi-directional biosphere-atmosphere exchange of ammonia. *Quarterly*
928 *Journal of the Royal Meteorological Society*, 127, 815–833.
- 929 Nowak, J. B., Neuman, J. A., Bahreini, R., Brock, C. A., Middlebrook, A. M., Wollny, A. G., ...
930 Fehsenfeld, F. C. (2010). Airborne observations of ammonia and ammonium nitrate
931 formation over Houston, Texas. *Journal of Geophysical Research Atmospheres*, 115(22), 1–
932 12. <https://doi.org/10.1029/2010JD014195>
- 933 Ostro, B., Hu, J., Goldberg, D., Reynolds, P., Hertz, A., Bernstein, L., & Kleeman, M. J. (2015).
934 Associations of mortality with long-term exposures to fine and ultrafine particles, species
935 and sources: results from the California teachers study cohort. *Environmental Health*
936 *Perspectives*, 123(6), 549–556. <https://doi.org/10.1289/ehp.1408565>
- 937 Paulot, F., Jacob, D. J., Pinder, R. W., Bash, J. O., Travis, K., & Henze, D. K. (2014). Ammonia
938 emissions in the United States, European union, and China derived by high-resolution
939 inversion of ammonium wet deposition data: Interpretation with a new agricultural

- 940 emissions inventory (MASAGE_NH3). *Journal of Geophysical Research*, 119(7), 4343–
941 4364. <https://doi.org/10.1002/2013JD021130>
- 942 Pinder, R. W., Walker, J. T., Bash, J. O., Cady-Pereira, K. E., Henze, D. K., Luo, M., ...
943 Shephard, M. W. (2011). Quantifying spatial and seasonal variability in atmospheric
944 ammonia with in situ and space-based observations. *Geophysical Research Letters*, 38(4),
945 1–5. <https://doi.org/10.1029/2010GL046146>
- 946 Pollack, I. B., Lindaas, J., Robert Roscioli, J., Agnese, M., Permar, W., Hu, L., & Fischer, E. V.
947 (2019). Evaluation of ambient ammonia measurements from a research aircraft using a
948 closed-path QC-TILDAS operated with active continuous passivation. *Atmospheric*
949 *Measurement Techniques*, 12(7), 3717–3742. <https://doi.org/10.5194/amt-12-3717-2019>
- 950 Rasmussen, C. (2018). Farewell to a Pioneering Pollution Sensor. Retrieved June 3, 2020, from
951 NASA Jet Propulsion Laboratory website:
952 <https://www.jpl.nasa.gov/news/news.php?feature=7061>
- 953 Scarino, A. J., Obland, M. D., Fast, J. D., Burton, S. P., Ferrare, R. A., Hostetler, C. A., ...
954 Harper, D. B. (2014). Comparison of mixed layer heights from airborne high spectral
955 resolution lidar, ground-based measurements, and the WRF-Chem model during CalNex
956 and CARES. *Atmospheric Chemistry and Physics*, 14(11), 5547–5560.
957 <https://doi.org/10.5194/acp-14-5547-2014>
- 958 Schiferl, L. D., Heald, C. L., Damme, M. Van, Clarisse, L., Clerbaux, C., Coheur, P. F., ...
959 Eilerman, S. J. (2016). Interannual variability of ammonia concentrations over the United
960 States: Sources and implications. *Atmospheric Chemistry and Physics*, 16(18), 12305–
961 12328. <https://doi.org/10.5194/acp-16-12305-2016>
- 962 Seinfeld, J. H., & Pandis, S. N. (2016). *Atmospheric Chemistry and Physics: From Air Pollution*
963 *to Climate Change, 3rd Edition*. Hoboken, NJ: John Wiley & Sons.
- 964 Shephard, M. W., & Cady-Pereira, K. E. (2015). Cross-track Infrared Sounder (CrIS) satellite
965 observations of tropospheric ammonia. *Atmospheric Measurement Techniques*, 8(3), 1323–
966 1336. <https://doi.org/10.5194/amt-8-1323-2015>
- 967 Shephard, M. W., Cady-Pereira, K. E., Luo, M., Henze, D. K., Pinder, R. W., Walker, J. T., ...
968 Clarisse, L. (2011). TES ammonia retrieval strategy and global observations of the spatial
969 and seasonal variability of ammonia. *Atmospheric Chemistry and Physics*, 11(20), 10743–
970 10763. <https://doi.org/10.5194/acp-11-10743-2011>
- 971 Someya, Y., Imasu, R., Shiomi, K., & Saitoh, N. (2019). Atmospheric ammonia retrieval from
972 the TANSO-FTS/GOSAT thermal infrared sounder. *Atmospheric Measurement Techniques*
973 *Discussions*, (April), 1–24. <https://doi.org/10.5194/amt-2019-49>
- 974 Sun, K., Cady-Pereira, K., Miller, D. J., Tao, L., Zondlo, M. A., Nowak, J. B., ... Hostetler, C.
975 A. (2015). Validation of TES ammonia observations at the single pixel scale in the San
976 Joaquin Valley during DISCOVER-AQ. *Journal of Geophysical Research Atmospheres*,
977 120(10), 5140–5154. <https://doi.org/10.1002/2014JD022846>
- 978 Sun, K., Tao, L., Miller, D. J., Pan, D., Golston, L. M., Zondlo, M. A., ... Zhu, T. (2017).
979 Vehicle Emissions as an Important Urban Ammonia Source in the United States and China.
980 *Environmental Science and Technology*, 51(4), 2472–2481.
981 <https://doi.org/10.1021/acs.est.6b02805>

- 982 Tao, L., Sun, K., Miller, D. J., Pan, D., Golston, L. M., & Zondlo, M. a. (2015). Low-power,
 983 open-path mobile sensing platform for high-resolution measurements of greenhouse gases
 984 and air pollutants. *Applied Physics B*, 153–164. <https://doi.org/10.1007/s00340-015-6069-1>
- 985 Tevlin, A. G., Li, Y., Collett, J. L., McDuffie, E. E., Fischer, E. V., & Murphy, J. G. (2017). Tall
 986 Tower Vertical Profiles and Diurnal Trends of Ammonia in the Colorado Front Range.
 987 *Journal of Geophysical Research: Atmospheres*, 122(22), 12,468–12,487.
 988 <https://doi.org/10.1002/2017JD026534>
- 989 Van Damme, M., Clarisse, L., Dammers, E., Liu, X., Nowak, J. B., Clerbaux, C., ... Coheur, P.
 990 F. (2015). Towards validation of ammonia (NH₃) measurements from the IASI satellite.
 991 *Atmospheric Measurement Techniques*, 8(3), 1575–1591. [https://doi.org/10.5194/amt-8-](https://doi.org/10.5194/amt-8-1575-2015)
 992 [1575-2015](https://doi.org/10.5194/amt-8-1575-2015)
- 993 Van Damme, M., Clarisse, L., Heald, C. L., Hurtmans, D., Ngadi, Y., Clerbaux, C., ... Coheur,
 994 P. F. (2014). Global distributions, time series and error characterization of atmospheric
 995 ammonia (NH₃) from IASI satellite observations. *Atmospheric Chemistry and Physics*,
 996 14(6), 2905–2922. <https://doi.org/10.5194/acp-14-2905-2014>
- 997 Van Damme, M., Clarisse, L., Whitburn, S., Hadji-Lazaro, J., Hurtmans, D., Clerbaux, C., &
 998 Coheur, P. F. (2018). Industrial and agricultural ammonia point sources exposed. *Nature*,
 999 564(7734), 99–103. <https://doi.org/10.1038/s41586-018-0747-1>
- 1000 Van Damme, M., Whitburn, S., Clarisse, L., Clerbaux, C., Hurtmans, D., & Coheur, P. F. (2017).
 1001 Version 2 of the IASI NH₃ neural network retrieval algorithm: Near-real-time and
 1002 reanalysed datasets. *Atmospheric Measurement Techniques*, 10(12), 4905–4914.
 1003 <https://doi.org/10.5194/amt-10-4905-2017>
- 1004 Volkamer, R., Baidar, S., & Thomas, D. (2019). *Patent No. 10379194*. United States.
- 1005 Von Bobruzki, K., Braban, C. F., Famulari, D., Jones, S. K., Blackall, T., Smith, T. E. L., ...
 1006 Nemitz, E. (2010). Field inter-comparison of eleven atmospheric ammonia measurement
 1007 techniques. *Atmospheric Measurement Techniques*, 3(1), 91–112.
 1008 <https://doi.org/10.5194/amt-3-91-2010>
- 1009 Wang, J. L., Zhang, Y. H., Shao, M., & Liu, X. L. (2006). The quantitative relationship between
 1010 visibility and mass concentration of PM_{2.5} in Beijing. *WIT Transactions on Ecology and*
 1011 *the Environment*, 86, 595–610. <https://doi.org/10.2495/AIR06059>
- 1012 Warner, J. X., Dickerson, R. R., Wei, Z., Strow, L. L., Wang, Y., & Liang, Q. (2017). Increased
 1013 atmospheric ammonia over the world's major agricultural areas detected from space.
 1014 *Geophysical Research Letters*, 44(6), 2875–2884. <https://doi.org/10.1002/2016GL072305>
- 1015 Warner, J. X., Wei, Z., Larrabee Strow, L., Dickerson, R. R., & Nowak, J. B. (2016). The global
 1016 tropospheric ammonia distribution as seen in the 13-year AIRS measurement record.
 1017 *Atmospheric Chemistry and Physics*, 16(8), 5467–5479. [https://doi.org/10.5194/acp-16-](https://doi.org/10.5194/acp-16-5467-2016)
 1018 [5467-2016](https://doi.org/10.5194/acp-16-5467-2016)
- 1019 Weinheimer, A. J., Walega, J. G., Ridley, B. A., Gary, B. L., Blake, D. R., Blake, N. J., ...
 1020 Collins, J. E. (1994). Meridional distributions of NO_x, NO_y, and other species in the lower
 1021 stratosphere and upper troposphere during AASE II. *Geophysical Research Letters*, 21(23),
 1022 2583–2586. <https://doi.org/10.1029/94GL01897>

- 1023 Whitburn, S., Van Damme, M., Clarisse, L., Bauduin, S., Heald, C. L., Hadji-Lazaro, J., ...
1024 Coheur, P.-F. (2016). A flexible and robust neural network IASI-NH₃ retrieval algorithm.
1025 *Journal of Geophysical Research: Atmospheres*, *121*(11), 6581–6599.
1026 <https://doi.org/10.1002/2016JD024828>
- 1027 Xu, W., Luo, X. S., Pan, Y. P., Zhang, L., Tang, A. H., Shen, J. L., ... Liu, X. J. (2015).
1028 Quantifying atmospheric nitrogen deposition through a nationwide monitoring network
1029 across China. *Atmospheric Chemistry and Physics Discussions*, *15*(13), 18365–18405.
1030 <https://doi.org/10.5194/acpd-15-18365-2015>
- 1031 Yacovitch, T. I., Herndon, S. C., Roscioli, J. R., Floerchinger, C., McGovern, R. M., Agnese, M.,
1032 ... Kolb, C. E. (2014). Demonstration of an ethane spectrometer for methane source
1033 identification. *Environmental Science and Technology*, *48*(14), 8028–8034.
1034 <https://doi.org/10.1021/es501475q>
- 1035 Zhang, L., Chen, Y., Zhao, Y., Henze, D. K., Zhu, L., Song, Y., ... Huang, B. (2018).
1036 Agricultural ammonia emissions in China: Reconciling bottom-up and top-down estimates.
1037 *Atmospheric Chemistry and Physics*, *18*(1), 339–355. [https://doi.org/10.5194/acp-18-339-](https://doi.org/10.5194/acp-18-339-2018)
1038 [2018](https://doi.org/10.5194/acp-18-339-2018)
- 1039 Zhu, L., Henze, D. K., Cady-Pereira, K. E., Shephard, M. W., Luo, M., Pinder, R. W., ... Jeong,
1040 G. R. (2013). Constraining U.S. ammonia emissions using TES remote sensing observations
1041 and the GEOS-Chem adjoint model. *Journal of Geophysical Research Atmospheres*, *118*(8),
1042 3355–3368. <https://doi.org/10.1002/jgrd.50166>
- 1043 Ziereis, H., & Arnold, F. (1986). Gaseous ammonia and ammonium ions in the free troposphere.
1044 *Nature*, 503–505.
- 1045